

instituteofaviation
warsaw, since 1926



REVIEW OF AERONAUTICAL FATIGUE INVESTIGATIONS IN POLAND (2017 – 2018)

by

Antoni Niepokólczycki

Institute of Aviation, Warsaw, POLAND
(Investigations in Civil Aviation)

and

Krzysztof Dragan & Marcin Kurdelski

Air Force Institute of Technology, Warsaw, POLAND
(Investigations in Military Aviation)

36th Conference of the International Committee on Aeronautical Fatigue and Structural
Integrity, Kraków, Poland, June 3 - 4, 2019

Approved for Public Release

TABLE OF CONTENT

INVESTIGATIONS IN CIVIL AVIATION	3
JOINTS	3
Fatigue Life Prediction Model for Riveted Joints	3
Experimental Validation of Riveting Process FE Simulation	4
Comparison of Rivet Hole Expansion for Protruding Rivets: Universal and with Compensator.....	10
MATERIALS TESTING	12
Multiaxial Fatigue Behavior of 30HGSA Steel under Cyclic Tension-Compression and Reversed Torsion	12
The Influence of Low and High-cycle Fatigue on Dislocations Density and Residual Stresses in Inconel 718.....	12
The Hardening in Alloys and Composites and its Examination with a Diffraction and Self- Consistent Model.....	14
Calibration of the Ductile Failure Criterion for Nickel-Based Superalloys Taking into Account the Localization of the Strain	23
OTHER WORKS	33
Study of Load Spectrum occurring in the course of photogrammetric missions of the UAV	33
The Fatigue Life of Cables in Aircraft Flight Control Systems	35
Conception of Modular Test Stand for Fatigue Testing of Aeronautical Structures	42
INVESTIGATIONS IN MILITARY AVIATION	45
STRUCTURAL LOAD / USAGE / HEALTH MONITORING	45
Operational Load Monitoring System for Su-22UM3K fighter - bomber.....	45
Concept of Health Monitoring System for Mi-8 Helicopter with Integrated Sensors	46
SHM application to Remotely Piloted Aircraft Systems - SAMAS	47
FULL SCALE TESTING	51
Evaluation of the suitability of a strain-gauge method for measuring deformations within the fatigue tests of aviation composite structures	51
ADHESIVELY BONDED STRUCTURES	54
The repair design and technology of metal rotor blades for Mi family helicopter – the approach with the usage of reverse engineering.....	54
NON-DESTRUCTIVE EVALUATION	56
Analysis of Adhesive Disbond Occurrences in Rotor Blades of Mi-2 Helicopters	56
MODELLING	58
Gradient Material Model in Analysis of Mechanical Joints	58

INVESTIGATIONS IN CIVIL AVIATION

JOINTS

Fatigue Life Prediction Model for Riveted Joints

The research team of the Faculty of Mechanical Engineering and Robotics at the University of Science and Technology (AGH) in Kraków led by Professor Małgorzata Skorupa developed a fatigue life prediction model for riveted joints. A specific focus of the work was generic riveted lap joints representative of the aircraft fuselage skin connections. Because of extremely complex determinants of the fatigue behavior of riveted joints, both the fatigue life and crack growth prediction approaches must be strongly empirical to account for phenomena that are either not well understood or too complicated to be covered analytically. With the proposed model it is assumed that the fatigue life of a joint is governed by the local stress amplitude at the rivet hole in the critical rivet row expressed as:

$$\sigma = S \cdot (\alpha_{BP}(1 - R_{TR})K_{f,BP} + \alpha_{BR}\alpha_{FR}R_{TR} \cdot K_{f,BR} + \alpha_b k_b \cdot K_{f,b}) \quad (1)$$

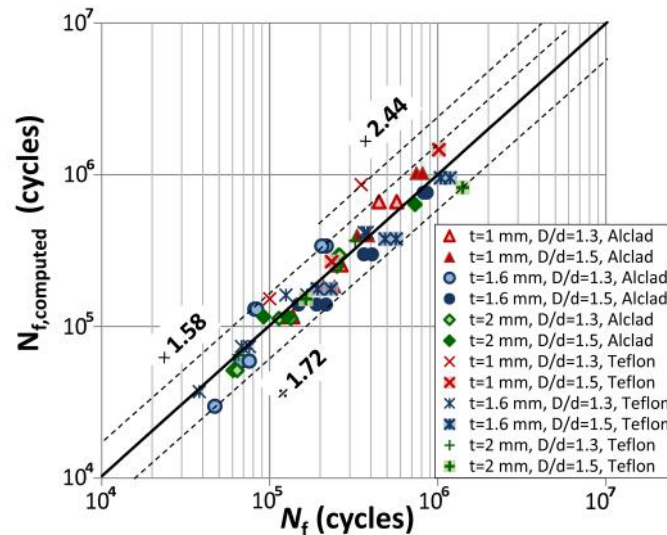
where S is the applied stress level, $K_{f,BP}$, $K_{f,BR}$, and $K_{f,b}$ are the fatigue notch factors for a finite width plate with open hole under remote tension, pin loading, and pure in-plane bending respectively, $R_{TR}=T_{TR}/P$ is the transfer load ratio (T_{TR} – transfer load, P – applied load), $k_b=S_b/S$ is the bending factor (S_b - nominal stress due to secondary bending), α_{BP} , α_{BR} and α_b are the rivet hole expansion dependent coefficients, and the α_{FR} coefficient accounts for the contribution of frictional forces to load transmission.

The preparatory experimental and analytical studies that were a basis for the model formulation are presented in refs [1 - 4]. The derivation of the k_b factor and the R_{TR} ratio was addressed in refs [1] and [2] respectively. A dependency of the α_{BP} , α_{BR} and α_b coefficients on rivet hole expansion and the adequacy of the K_f coefficients available in the literature was determined from comparative fatigue tests on coupons with a central hole open and filled with an interference-fit pin, and on un-notched coupons under loadings replicating the effect of each of the three loading cases considered in Eq. 1 [3]. In the context of the considered fatigue life prediction model, the observed results implied that in the range of rivet hole expansion values representative for the aircraft industry practice the notch effect could be neglected in the case of the bypass load and secondary bending [4]. Consequently, Eq. 1 could be reduced to the form:

$$\sigma = S \cdot (1 - R_{TR} + \alpha_{BR}\alpha_{FR}R_{TR} \cdot K_{f,BR} + k_b)$$

The derivation of the α_{BR} coefficient and its dependency on several quantities related to the amount of rivet squeezing, and thus representative of the riveted process is provided in ref. [4]. An experimental study of the friction force evolution on the faying surface of the lap joint under cyclic loading is also presented in ref. [4]. This study indicated that frictional forces on the Alclad contact surface caused by fretting could significantly or even fully release the bearing load on the rivet hole. In contrast, for the joints with the Teflon foil inserted between the sheets load transmission occurred solely by the bearing pressure. In view of the above observations the α_{FR} coefficient was determined by comparing results of fatigue tests of riveted lap joint specimens with the Alclad and Teflon interface, and a dependency of α_{FR} on the magnitude of rivet squeezing could be established [4].

The adequacy of the model is substantiated by results shown in the figure below which shows a very good agreement between the predicted and observed fatigue lives for over 60 riveted lap joint specimens characterized by various amounts of the rivet squeeze represented in the legend by the D/d ratio, where D – rivet driven head diameter, d – rivet shank diameter, different sheet thicknesses and two different faying surface conditions.



The validity of fatigue life prediction models for riveted joints developed so far is limited to cases when the riveting process and the faying surface condition for the reference joint and for the actual joint are similar. However, the criterion for the riveting process similarity cannot be formulated in a precise way. In contrast, the model considered above requires essentially no constraints on its applicability, and thus it represents a considerable step forward in the prediction methodology for mechanically fastened joints.

- [1] Skorupa M, Korbel A, Skorupa A, Machniewicz T. Observations and analyses of secondary bending for riveted lap joints. *Int. J. Fatigue* 2015;72:1-10.
- [2] Skorupa M, Machniewicz T, Skorupa A, Korbel A. Effect of load transfer by friction on the fatigue behaviour of riveted lap joints. *Int J Fatigue* 2016;90:1-11.
- [3] Skorupa M, Machniewicz T, Skorupa A, Korbel A. Fatigue strength reduction factors at rivet holes for aircraft fuselage lap joints. *Int J Fatigue* 2015;80:417-25.
- [4] Skorupa M, Machniewicz T, Skorupa A, Korbel A. (2017) Fatigue life predictions for riveted lap joints. *Int J Fatigue*; 94: 41-57.

Experimental Validation of Riveting Process FE Simulation

Introduction

Since the Aloha Airline accident in 1988, the fatigue characteristics of riveted joints have been subjected to numerous investigations and analyses. Fatigue is the most common reason of failure in aerospace structures and very often cracks initiate near fastener holes [1]. In addition to heightening the risk of catastrophic failure, fatigue behavior strongly influences the service cost of an aircraft since it determines the airframe lifespan as well as types and frequency of inspections.

Fatigue life of riveted joints depends strongly on the rivet type and riveting technology used. For identical specimens and loads, the number of cycles to failure can differ significantly [2] – [4]. Residual stresses after riveting play a crucial role in fatigue cracks nucleation and growth [5], [6]. Local maximum and minimum peak stresses at critical locations are used to estimate the fatigue life of riveted joints by both numerical analyses and a number of semi-empirical approaches [5]–[7]. In joined elements, the riveting process induces a complex stress state that analytical methods cannot properly predict. Numerical methods, especially Finite Element (FE) calculations, enable researchers to determine the stress distribution in the entire joint, also at the faying surface, where cracks usually nucleate. This location is practically inaccessible to experimental methods. It is characteristic of the FE analysis that input data (e.g. material models) can strongly influence the results, possibly leading to obtaining unrealistic values. In order to ensure that the model accurately represents the reality, its validation is necessary.

The work focused on the validation process of the riveting FE simulations. Two types of rivets were analyzed, i.e. the universal rivet according to the MS20470 standard and the countersunk rivet according to the NAS1097 standard. Rivets were made of 2117-T4 alloy with diameter equal to 4 mm. Sheets made of 2024-T3 alloy with thickness equal to 1.5 mm were selected. At first, force-displacement curves of the press punch obtained in the experiments and calculations were compared. In the next step, validations concerns strains near a driven head recorded by strain gauges and determined in calculations.

Finite Element Models

The models of joints with two sheets and one rivet were prepared for the riveting process simulation based on previous works [8] – [10]. Four nodes linear elements for axisymmetric analysis were used. Each model consisted of three deformable contact bodies (a rivet and two sheets) and three rigid contact bodies (a hold-on, a punch and a support under the bottom sheet). The radius of sheets was equal to 30 mm. The hold-on and the support were fixed while the punch was moving vertically forming a driven head until the force reached the assumed value, whereupon it was released. The central parts of the models are shown in Fig.1. Each model consisted of about 2 500 – 3000 elements.

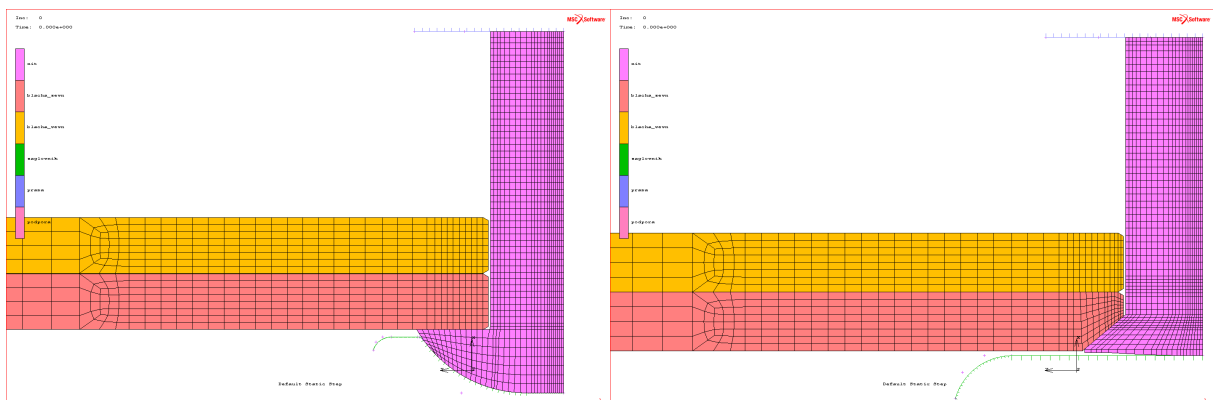


Figure 1. Central part of the FE models of joints

The quasi-static simulations of riveting were performed with the use of the implicit nonlinear algorithm (MSC Marc). The elasto-plastic material behaviour as well as contact phenomena were taken into account. The values of friction coefficients were assumed based on [11] and in the case of kinematic friction were equal to 0.34 for aluminium pairs and 0.15 for steel-aluminium interactions. In the case of static friction, coefficients values were 1.24 times higher. Material models are presented in Fig. 2. Model of the 2024-T3 alloy (sheet) was

developed based on the material test, while in the case of the 2117-T4 alloy (rivet), the model was taken from [11].

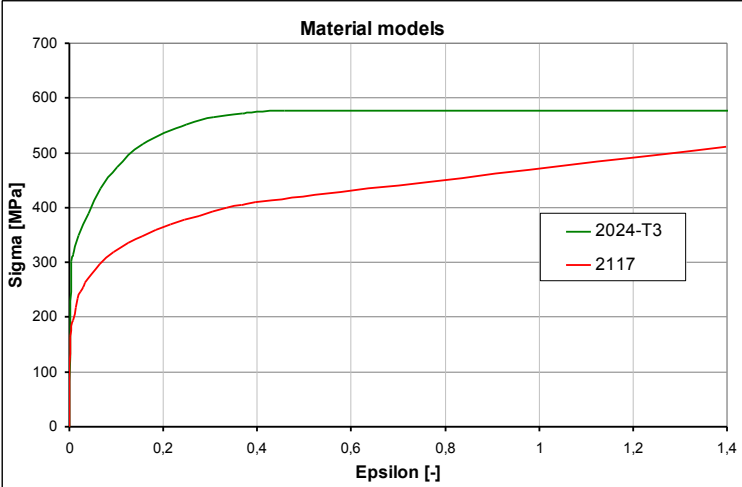
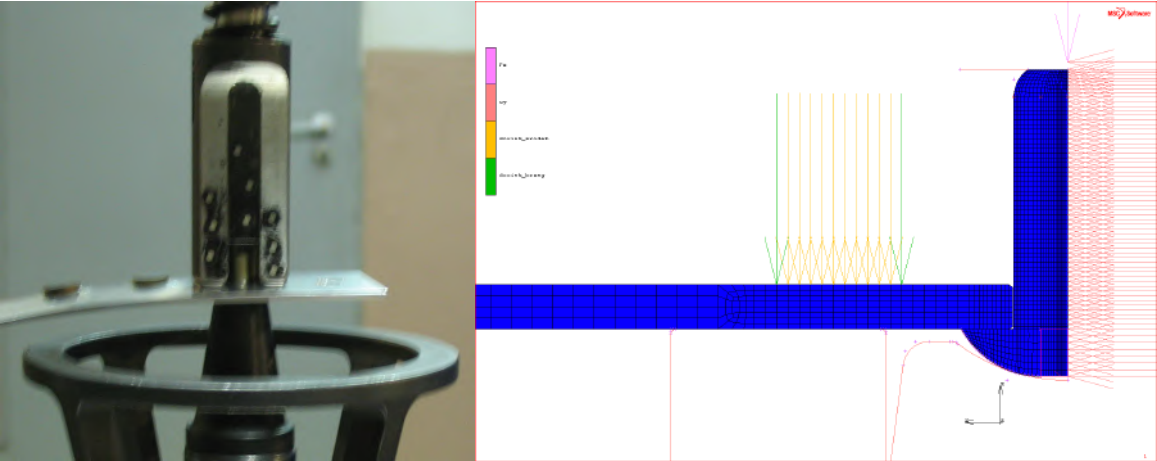


Figure 2. Material models

Force-Displacement Curves

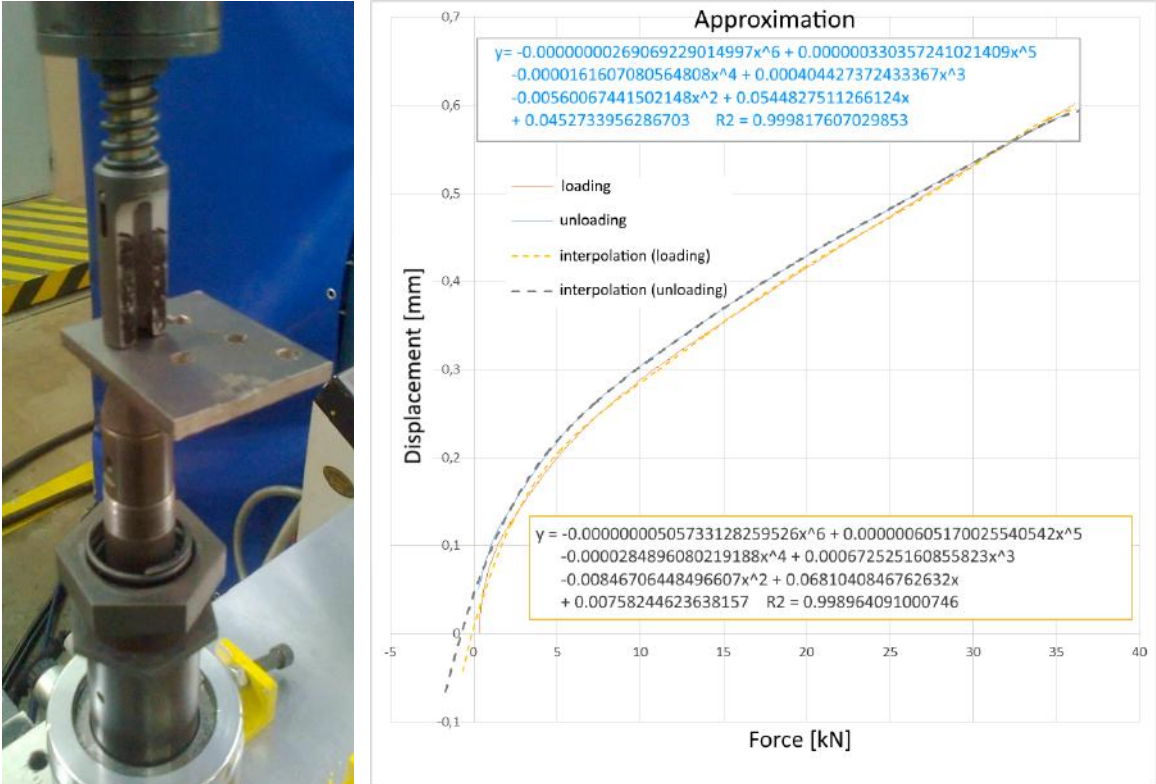
In order to validate the 2117-T4 alloy (rivet) material model, tests of squeezing rivets for both analyzed types were performed on the MTS 312/68 testing machine. Each rivet was inserted into a hole in a one sheet to prevent it from rotating and squeezed with force equal to 36 kN. The test was repeated three times for both rivet types. The controller of the testing machine recorded squeezing forces and punch displacements. The FE models described above were modified to represent these tests. Figure 3 shows the experiment and the modified FE model of the universal rivet.



a) b) Figure 3. Squeezing rivets, a) experiment, b) FE model

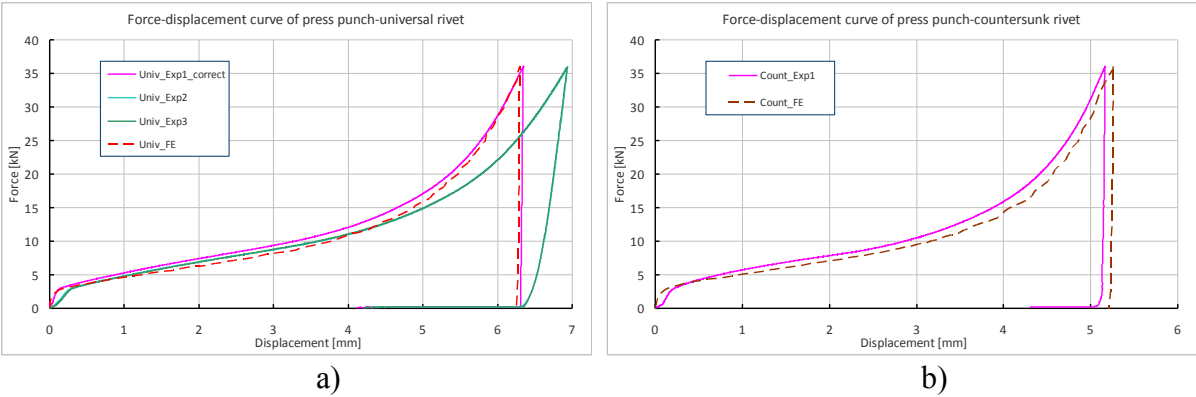
The displacements were measured by the testing machine controller and include also translations resulting from the flexibility and clearances of elements mounted into the testing machine. A piece of steel was squeezed in the stand to measure these additional displacements (Figure 4). The obtained force-displacement curve was interpolated by a polynomial and used for making a correction of the force-displacements curves obtained for rivet squeezing (for

each point, the displacement measured during squeezing the steel plate was subtracted from the displacements measured during squeezing the rivet with a particular force value).



a) b)
Figure 4. Measurement of stand flexibility, a) experiment, b) obtained curves

Figure 5 presents comparison of force displacements curves obtained experimentally and through the FE calculations for both types of rivets. In the case of the universal rivet (Fig. 5a), the curve without correction was also presented. Experimental curves for three specimens were practically identical for both cases. Flexibility and clearances of the test stand caused distinct additional displacements recorded by the controller of the testing machine. After the correction described above, a good agreement between experiments and numerical analyses was obtained.



a) b)
Figure 5. Force displacements curves obtained experimentally and in FE calculations, a) universal rivet, b) countersunk rivet

Strain Distribution Near Driven Head

The next step in the models' validation involved comparing the strain distribution around the rivets' driven heads. The results of numerical calculations were compared against the data obtained during the strain gauge measurements [10]. Each specimen consisted of two bare sheets (2024-T3, $t=1.6$ mm) and six rivets (2117T4, ϕ 4 mm, universal or countersunk head). Around the central rivet, the Vishay strip gauges patterns type 020MT and 020 PF were applied onto the driven head side to measure radial and tangential strains respectively. Figure 6 presents the specimens geometry and arrangement of strain-gauges around the central rivet.

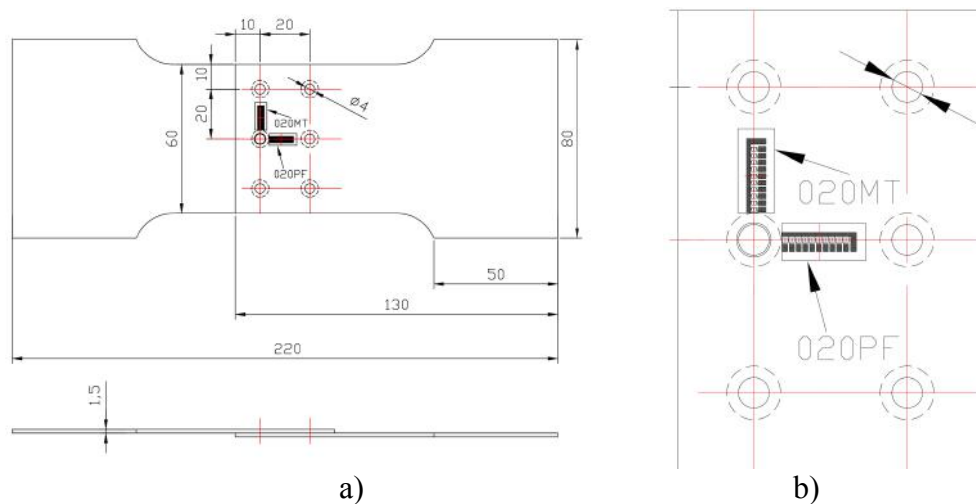


Figure 6. Specimen configuration, a) geometry, b) strain gauges arrangement

Riveting was performed with a force controlled by the testing machine. For all rivets, the driven head diameter was about 1.7 times greater than the rivet shank diameter. The squeezing force was equal to 25 kN and 24.5 kN for the universal rivet and the countersunk rivet, respectively. At first, all rivets except the central one were successively squeezed, then during the last riveting, strains around the central hole were recorded. Measurements were performed on five specimens for each of the rivet type.

The recorded strains were compared against the results of the FE simulations. Due to axisymmetric analysis, each of the FE model represents a joint with circular sheets and a single rivet. Previous analysis shows that such simplification is appropriate [8]. Figures 7-8 presents strain distributions around driven heads for both rivet types determined during the measurements and the FE simulations. Experimental curves were designated with a specimen number.

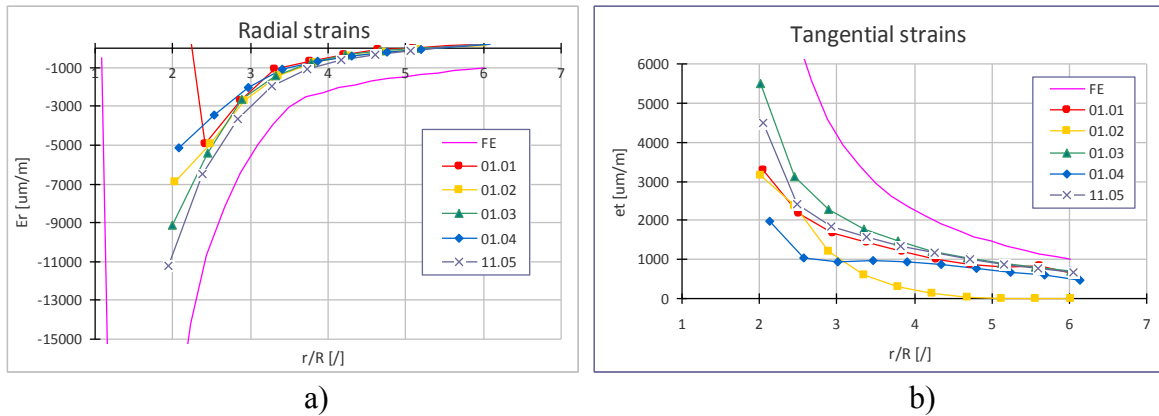


Figure 7. Strain distribution around driven head for universal rivet a) radial, b) tangential, r -distance from rivet axis, R -rivet shank radius

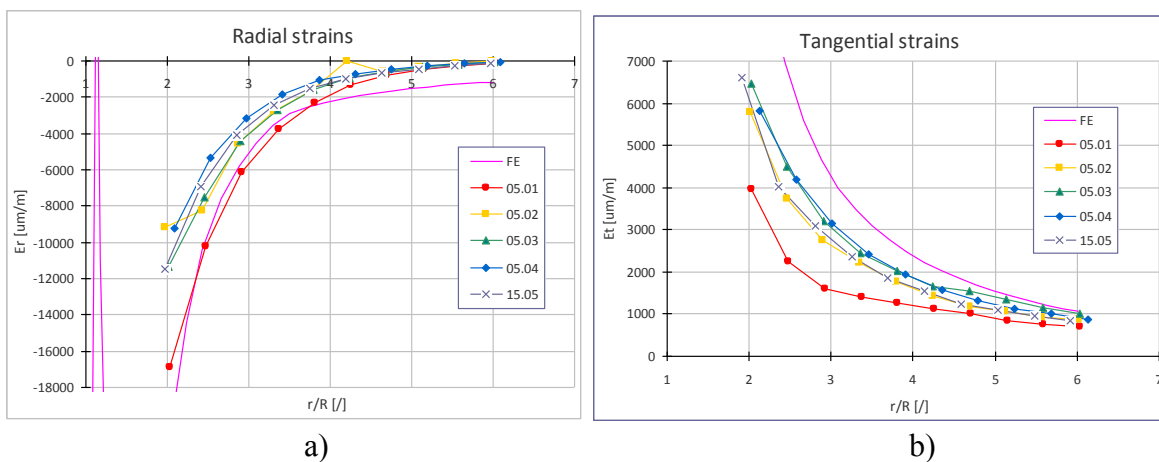


Figure 8. Strain distribution around driven head for countersunk rivet a) radial, b) tangential, r -distance from rivet axis, R -rivet shank radius

In the case of the countersunk rivet, quite good correlations were obtained, especially for radial strains. Results of numerical simulation for the universal rivet were substantially higher than measured values. The main difference between the analysed FE models was the geometry. According to the experiment, in the FE simulations the squeezing force value in the case of the universal rivet was slightly higher than for the countersunk rivet. The sheets used in the experiment were the same for both cases. Rivets were made of the nominally identical alloy but were provided by various suppliers. Slight differences in material properties of used rivets probably is the reason of various level of correlation between simulation and experiment for analysed rivet types.

Conclusions

The paper presented the validation process of the riveting FE simulations. At first, the material model of rivet was validated with the use of the force–displacement curves of the press stamp. Because of the displacement measurement method, it was necessary to take into account the flexibility of the stand. The translations resulting from flexibility and clearances of the stand elements were measured and subtracted from the displacements measured during squeezing of the rivets. The magnitude of these corrections was found to be significant. After that, good correlation between the numerical simulations and the experiment was obtained for both rivet types.

At the second stage, strains around driven heads measured with the use of strip gauge patterns were compared with the results of the FE simulations. Quite good correlation was obtained for the countersunk rivet. In the case of the universal rivet, numerical results are significantly higher than measured values. Various levels of correlation of the experiments and FE simulations for the analysed rivet types probably result from material differences of the rivets. The presented study confirms that material characteristics are crucial in the case of FE simulations and a good correlation of calculation and experiment with respect to displacements do not ensure that numerically determined stress distribution will be correct.

References

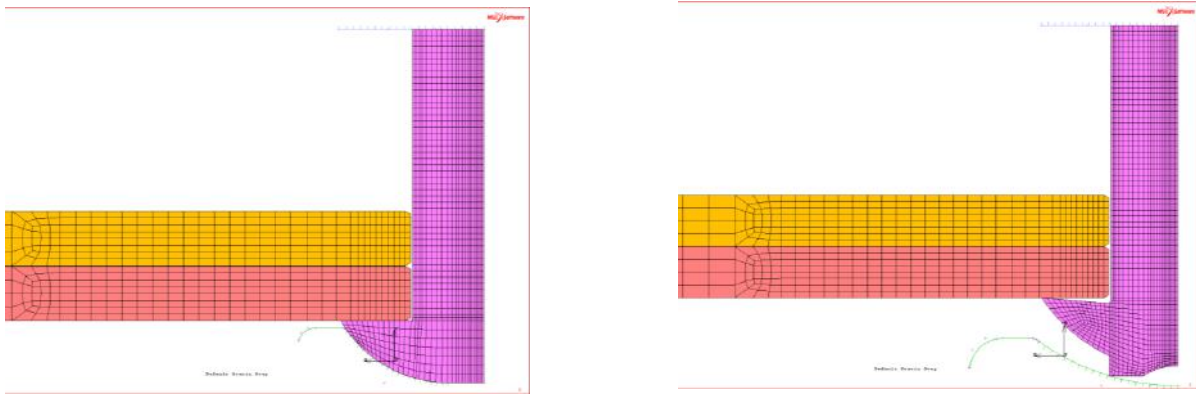
- [1] S. J. Findlay and N. D. Harrison, ‘Why aircraft fail’, *Mater. Today*, vol. 5, no. 11, pp. 18–25, Nov. 2002.
- [2] R. P. G. Müller and L. J. Hart-Smith, ‘Making fuselage riveted lap splices with 200-year crack-free-lives’, in *Fatigue in New and Aging Aircraft*, Edinburgh, Scotland, 1997, pp. 18–20.
- [3] M. Skorupa, A. Skorupa, T. Machniewicz, and A. Korbel, ‘Effect of production variables on the fatigue behaviour of riveted lap joints’, *Int. J. Fatigue*, vol. 32, no. 7, pp. 996–1003, Jul. 2010.
- [4] A. Lipski, ‘The Influence of The Degree of the Rivet Hole Sizing on the Fatigue Life’, *Fatigue Aircr. Struct.*, vol. 2012, no. 4, pp. 64–69, 2012.
- [5] R. P. G. Müller, ‘An experimental and analytical investigation on the fatigue behaviour of fuselage riveted lap joints’, Delft University of Technology, Delft, 1995.
- [6] A. Skorupa and M. Skorupa, *Riveted Lap Joints in Aircraft Fuselage: Design, Analysis and Properties*, 2012th ed. Dordrecht ; New York: Springer, 2012.
- [7] J. J. Homan and A. A. Jongebreur, ‘Calculation method for Predicting the Fatigue Life of Riveted Joints’, in *Durability and structural integrity of airframes*, Stockholm, Sweden, 1993, vol. 1, pp. 175–190.
- [8] W. Wronicz and J. Kaniowski, ‘Experimental and Numerical Study of Strain Progress During and After Riveting Process for Brazier Rivet and Rivet with Compensator - Squeezing Force and Rivet Type Effect’, *Fatigue Aircr. Struct.*, vol. 2011, no. 3, pp. 166–190, 2011.
- [9] W. Wronicz, ‘Comparison of Residual Stress State on Sheets Faying Surface after Standard and NACA Riveting-Numerical Approach’, *Fatigue Aircr. Struct.*, vol. 2016, no. 8, pp. 116–126, 2016.
- [10] W. Wronicz, J. Kaniowski, M. Malicki, P. Kucio, and R. Klewicki, ‘Experimental and numerical study of NACA and conventional riveting procedure’, *Fatigue Aircr. Struct.*, vol. 2017, no. 9, pp. 157–170, 2017.
- [11] J. Fárek, ‘FE-Modelling Methodology of Riveted Joints’, *Czech Aerosp. Proc. J. Czech Aerosp. Res.*, vol. 2010, no. 3, pp. 12–16, 2010

Comparison of Rivet Hole Expansion for Protruding Rivets: Universal and with Compensator

Fatigue is one of the main reasons for airframe failure and cracks initiate very often near rivet holes. Although knowledge about fatigue in riveted joints has been significantly improved since the Aloha airlines accident, failures related to fatigue cracks along such joint

still happened. Riveting technology influences strongly fatigue of joint and a number of cycles to failure can vary more than twenty times for the same joint and load. One of the most influencing factors is a squeezing force level. During riveting, a rivet shank fills a hole and deforms sheets by expanding a hole. If the force is high enough, compressive radial and tangential stresses are generated around a hole. It is the same phenomena as in calibration (cold working) process used to increase a fatigue life of elements with holes. The holes' expansion, defined as an increase in diameter of a hole divided by its initial value, is the parameter that characterizes the degree of cold working. It can be used to assess a quality of a joint or even to estimate (together with other parameters) its fatigue life.

The work involved the numerical analysis of the hole expansion during riveting for two types of protruding rivets, namely the universal rivet according to the MS20470 standard and the brazier rivet with a compensator according to the Russian branch standard OST 1 34040-79. The joints analyzed consisted of two sheets with a thickness of 1.5 mm made of the 2024-T3 alloy and the rivet with a diameter of 4 mm made of the 2117-T4 alloy. FE simulations of a quasi-static riveting were performed with the use of the axisymmetric models. Figure below presents the central part of the models.



Central part of FE models of joints, left: universal rivet, right: rivet with compensator

The compensator has a small protrusion on the rivet head which is pressed into it during installation. This concept improves the hole expansion on the manufactured head side and increases fatigue life of a joint.

The results of the performed FE simulations show that the hole expansion under the driven head ($z/t \approx 2$) is on the similar level for both cases, while under the manufacture head ($z/t \approx 0$) the rivet with a compensator caused much higher expansion. At the mating surface ($z/t \approx 1$) expansion is significantly higher also for this rivet type, what is important since this is usually a critical area, where fatigue cracks initiate. Another advantage of the rivet with a compensator is the fact, that the hole expansion is much more uniform along the thickness.

Rivets with a compensator were developed for the other alloy (Polish PA25/Russian W65) and lower squeezing force. Probably, a further improvement of its characteristic is possible by optimization its geometry for configuration typical for commonly used rivets. The analysis as well as results of fatigue tests convinces the author that the concept of rivet with a compensator has significant potential to improve fatigue properties of joints practically without increasing costs.

MATERIALS TESTING

Multiaxial Fatigue Behavior of 30HGSA Steel under Cyclic Tension-Compression and Reversed Torsion

The 30HGSA steel is a very attractive metal due to its high hardenability, strength and resistance to wear for element production in many industries, including aerospace engineering. Those parameters can be achieved only in a process of thermal treatment, which includes hardening and tempering. Its strength properties depend on element's dimensions, so it is usually used for elements with thicknesses not exceeding 60 mm. The 30HGSA steel is often a material of choice for parts of riveted constructions and manufacturing of heavy loaded parts such as spindles, levers, gears, flanges, bushings, axles, shafts, compressor blades etc. In the aviation industry it has a wide application in the production of airframes, engines and its components like struts, and chassis shaving.

Most of those elements are subjected to a complex cyclic loading, which can result in fatigue damage. Therefore, to correctly construct parts, it is crucial to examine the fatigue behavior of the 30HGSA steel. In the work the behavior fatigue under cyclic in-phase tension-compression and torsion for 30HGSA steel for cylindrical specimens was examined. Tests were conducted at room temperature in ambient air with the biaxial MTS servo-hydraulic machine. The three types of experiments: (i) – uniaxial symmetrical cyclic compression-tension loading for high-cycle range, (ii) - cyclic reverse torsion high-cycle loading, (iii) – combined cyclic tension/compression and reverse torsion loading. The fatigue limits data measured in (i) and (ii) loading condition are approximately comparable to Huber-Mises-Hencky (HMH) criterion. The measured fatigue limit under cyclic torsion loading was at 60% of the stress amplitude determined for cyclic tension-compression loading.

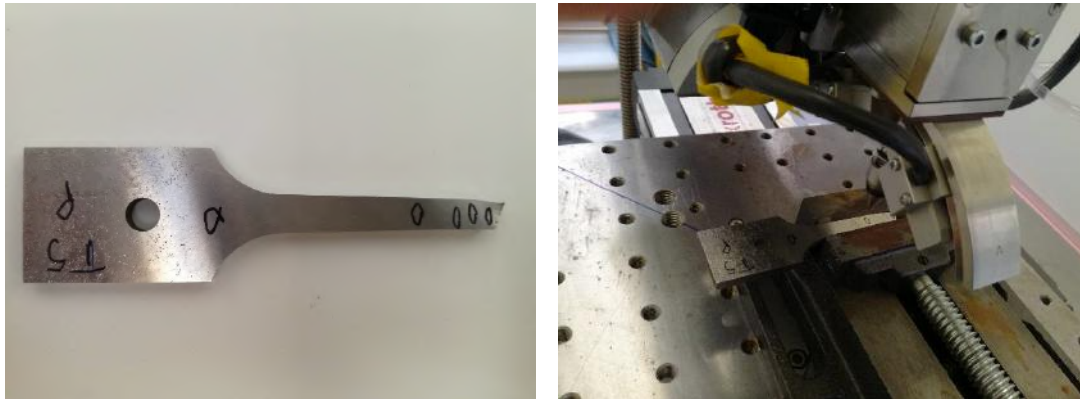
Based on the experimental data, the 'σ-τ curves' – limit curves (obtained for a fixed number of cycles) were determined. The results were later used to perform the analysis with two failure criteria namely Gough-Pollard (GP) and Debski-Golos-Debski (DGD) for the case of complex cyclic loading. The comparison of obtained data with analyzed criteria shown relatively good agreement between them.

The Influence of Low and High-cycle Fatigue on Dislocations Density and Residual Stresses in Inconel 718

The fatigue phenomena, as being one of the crucial importances for aircraft exploitation life and the passengers' safety, were investigated with different methods for years. The one of the most important is to determine the fatigue state of the material and subsequently the moment of fatigue crack initiation. Many authors investigated the fatigue induced material structural transformations with different methods i.e.: scanning electron microscopy, electron transmission microscopy, optical microscopy and two-beam interferometry or/and with modeling. Nowadays, as the possibilities of diffraction methods with different types of radiation were developed, the conjoining of the diffraction image with the changes in the material structure can be applied to investigate the fatigue process in materials.

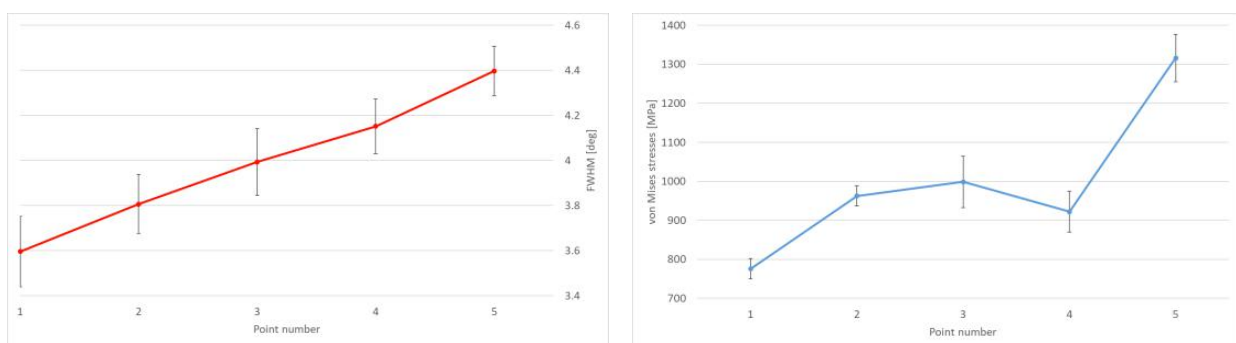
The aim of work was to find out the relationship between the stress and dislocation density evolution applying the X-ray diffraction methods. The dislocations and the level of their density are responsible factors for the plastic deformation in metals. They multiply and recognize during deformation and as a result of cyclic loading so their evolution can be valuable information for investigation of fatigue strength.

The diffraction methods are the only one non-destructive method for stress values investigations as well as one of highly versatile technique for quantitative analysis of grain level deformation. In this study X-ray diffraction is employed to acquire the information about the evolution of elastic lattice strains and changes in dislocation density after fatigue cycling of Inconel 718 alloy. The one of the examined specimen is presented in figure below.



left): The Inconel 718 specimen after fracture in fatigues test, and right): the same specimen during the X-ray diffraction experiment

In principle the discussion of the experimental results concerns the fatigue procedures. X-ray diffraction has been employed to assess the damage level under low and high cycle fatigue conditions. This evaluation was supposed to be performed by correlation of X-ray diffraction data with the microstructural changes in the material caused by various fatigue regimes. The objectives of the work were achieved by two X-ray diffraction techniques: the analysis of residual stresses changes after fatigue tests and the description of changes of full width at half maximum (FWHM) of diffraction peaks which is a measure of dislocation changes density. The figures below present some exemplary changes of residual stresses and the changes in peaks broadening for different points of fatigue specimen after fracture.



left): Von Mises stress values and right): changes of FWHM values for different points with respect to the distance form the fracture.

The significant changes of both, the effective stress values as well as the changes of the diffraction peaks can be observed. In the work, a series of X-ray diffraction measurements on

samples of Inconel 718 alloy were carried out. Thanks to that the limitations of this approach could be discussed.

The Hardening in Alloys and Composites and its Examination with a Diffraction and Self-Consistent Model

Introduction

A number of different factors affect the mechanism of hardening of alloys and composites: the phase composition, alloying agents, density of dislocation, morphology of precipitations resulting from a heat treatment applied or the grain size, and, naturally, the presence of reinforcement in composites [3]. Each of the above-mentioned determinants influences the ability to move dislocations, which in turn changes the value of the yield strength and the ductility of the material. Firstly, the strengthening mechanisms, both in the alloy and in the composite of two types were described. Then, the experimental setup was specified and the experimental results were discussed. This make it possible to determine the type of hardening in the composites examined.

Hardening in alloys

The hardening of the alloy due to the *presence of alloying elements* is usually not very influencing and can play an important role only if its clusters are formed in the body of the material. Designating the distance between the clusters of alloying elements as l , let's assume that each cluster contains n atoms, so the slip plane covered by the cluster is equal to nb^2 , where b is the vector of Burgers' displacements. Under these assumptions, the concentration of foreign atoms in the cluster will be [4]:

$$c = \frac{nb^2}{l^2} \quad \text{eq. 1}$$

The atoms of every cluster constrain the movement of dislocations in the slip plane and force the deflection. If the load applied rises, the deflection radius decreases while the force acting on every cluster increases. When assuming $r = \frac{l}{2}$ as the condition for the passing of the dislocation through the cluster, the shear stress will be [4]:

$$\tau_s = \frac{2\mu b}{l} \quad \text{eq. 2}$$

where μ is the shear modulus.

The increase in critical resolved shear stress (CRSS) will be the result of eq. 1 and eq. 2 combined:

$$\Delta\tau = 2\mu \sqrt{\frac{c}{n}} \quad \text{eq. 3}$$

The grain size is another factor affecting the strength of alloy. The impact of this factor is ruled by the empirical relationship i.e. the Hall-Petch equation:

$$\sigma_y = \sigma_i + \frac{k_y}{\sqrt{d}} \quad \text{eq. 4}$$

where:

σ_i – an average yield stress of a single grain,

k_y – the effectivity of impact made on the yielding point by the grain boundaries (most commonly: $0.1\text{MPa}\sqrt{m}$ [5]),

d – average grain size.

The precipitation hardening involves a wide range of structural phenomena developing in metal alloys. The heat treatment such dissolution, solution heat treatment and aging causes the particles in the alloy to harden. During the aging process, stable and metastable phases precipitate, which in turn gives different hardening effects [6]. The mean CRSS value becoming from the spheroidal, coherent inclusion into the metal matrix, whose volume is bigger than the molar volume of the matrix, is given by [4]:

$$\tau = 2\mu_0 \varepsilon f \quad \text{eq. 5}$$

where:

μ_0 – the shear modulus of a matrix,

ε – the precipitate – matrix misfit degree,

f – volume fraction of precipitates in the matrix.

If the distance between the precipitates in the slip plane is bigger than the minimal curvature radius (ϱ) of the dislocation deflection [4]:

$$\varrho = \frac{b}{4\varepsilon f} \quad \text{eq. 6}$$

the eq. 5 determines the macroscopic yield stress of a material.

If precipitate is supposed to affect the dislocation movement, the distance between precipitates (d) must meet the requirement that:

$$d \geq \frac{b}{4\varepsilon f} \quad \text{eq. 7}$$

The value of the critical resolved shear stress, required to move the dislocation through the coherent spherical precipitation particle, is given by:

$$\tau \geq \frac{f\gamma_p}{b} + \frac{\sqrt{6}f\gamma_s}{\pi r} \quad \text{eq. 8}$$

where:

γ_p – the inner precipitate boundary energy (after the dislocation passing),

γ_s – the interphases (precipitate and matrix) boundary energy,

r – average radius of spherical precipitate.

The first term of eq. 8 relates to the stress necessary to shear the precipitate. When the precipitate size increases, this term becomes dominate. The second term expresses the stress needed for producing an extra interphase boundary between the precipitate and the matrix [4].

Above case describe the case of precipitate for which on the boundary the planes and crystallographic directions are preserved, known as the coherent precipitate. Not coherent particles are introduced into the material intentionally through the process of dispersion hardening to strengthen the material. In this case, the dislocations movement is explained by the Orowan approach. According to this concept, dislocations can pass through the particles leaving circular loops around them if the applied stress is high enough. In this situation, the shear stress is given by [4]:

$$\tau = \tau_s + \frac{\mu_0 b}{4\pi} \Phi \ln \left(\frac{d - 2r}{2b} \right) \frac{2}{d - 2r} \quad \text{eq. 9}$$

where:

τ_s – matrix yield stress,

$\Phi = \frac{1}{2} \left[1 + \frac{1}{(1-\nu)} \right]$, and ν – Poisson's ratio,

d – average distance between particles in the slip plane,

r – spheroidal particle radius.

Hardening in metal matrix composites

In the case of the metal matrix composites, both phenomena described above can appear, i.e. these characteristics for precipitates in alloys as well as in materials with particles intentionally introduced. The strengthening mechanisms can be generally divided into two groups from the perspective of the plasticity beginning: joined with the internal stresses and connected to the matrix microstructure effects. The first type is associated with not uniform stress distribution between the reinforcement and the matrix. It causes change in stress level in the matrix as compared to the material with the reinforcement when the same stress is applied.

The effects connected with the microstructure of the matrix are: the evolution of dislocations, grain size of the matrix as well as the effects connected with the dispersive hardening [3].

Internal stresses

A relatively higher stiffness of the reinforcement particles as compared to the properties of the matrix causes the irregular distribution of stress applied to the material between the matrix and the reinforcement. Due to this phenomenon, the stress distribution is different in certain specific areas and points in the matrix. The reason is that, in the presence of the reinforcement, a very significant decrease in stress in the matrix appears as a result of load transfer from the matrix to the reinforcement. As the material has to fulfill the continuum conditions, the normal stress value on the interface reinforcement inclusion and the matrix have to be equal to the average stress value in the inclusion. On the other hand, experiments show that the yield stress of the composite material is not governed by the micro-yielding on the interface inclusion and matrix but rather by the achievement of the average stress value for the matrix [3], [7].

Matrix microstructure effects

The influence of the reinforcement on the strength of a composite as a whole is of bifold types. It affects the changes in the stress distribution but also the microstructural properties of the matrix.

The first type of composite hardening has the same origin as in the case of alloys: it is connected to the precipitations presence. Dislocations in metal matrix composites may have the origin of two types: in the load applied or in relaxation of residual thermal stresses. The case of residual thermal stresses was investigated by Arsenault et al. in [8] and [9]. The authors stated that the increase of dislocation density $\Delta\rho$ (as an outcome of punching of dislocation loops), could be described by the equation [7]:

$$\Delta\rho = \frac{\Delta\alpha\Delta T \cdot N \cdot A}{b} \quad \text{eq. 10}$$

where:

$\Delta\alpha$ – difference between thermal expansion coefficients of phases in the composite,

$\Delta\alpha\Delta T$ – thermal misfit strain,

N – number of particles,

A – total surface area of each particle,

b – Burgers vector.

It follows from the above equation that the dislocation density increases with the reduction of reinforcement particle size. The effect is significant especially for particles whose size is below $1\mu m$.

The change in the matrix strength combined with the dislocation density is given by [7]:

$$\Delta\sigma_{YM} \sim Gb\sqrt{\rho} \quad \text{eq. 11}$$

The other source of the composites strengthening is associated with the *grain size*. Its influence on the composite strength is given by the classical Hall-Petch formula (eq. 4). This

formula relates the change in the yield stress to the grain size. Substituting to the eq. 4 the appropriate values, i.e. $k_y = 0.1MPa\sqrt{m}$ and $d = 1\mu m$, the change in yield stress being the result of the fine grain size is about $100MPa$. Clyne and Withers [7] suggest that in practical cases it is few tens of MPa [7].

The last type of the MMC composites' strengthening described by Orowan, is caused by the resistance of the dislocation through the tightly positioned *particles of reinforcement*. In the MMC, sizes of reinforcement particles are relatively big and distances between them are large so this mechanism can be treated as negligible. It can, however, play a role in age-hardened materials where precipitates in the matrix appear. On the other hand, the impact of the reinforcement on the size and distribution of fine precipitates can be significant [7].

Material

The material used for the experimental investigation of strengthening mechanisms in metal matrix composites was an aluminum alloy matrix with a silicon carbide reinforcement; Al/SiC composite. Aluminum is a material of relatively low density and strength but with high ductility and thermal and electrical conductivity [10]. It is relatively easy to form [11], [12]. The limitation for pure aluminum application is defined by its comparably low strength, hardness, melting point ($658^\circ C$ [13]), stiffness and tribological properties [10], [14]. However, strength and hardness can be easily improved by alloying and heat treatment via solution hardening or/and the second phase hardening (e.g. precipitation hardening of Al-Cu alloys or silicon carbide particles hardening). The composite reinforced with the SiC particles was chosen for these investigations, because of significance of this kind of composites in the space-aviation applications [15].

The material examined in this work was produced by Materion Company with a unique method known as the BP process. This technique involves blending and compaction of mixed powder components [16]. Thanks to that technique the resulting composite possesses better mechanical properties, which is the main advantage of this method. These superior properties result from improved strength at the matrix/reinforcement interface [16]. The examined composite was combined from the 2124 aluminum alloy matrix and the SiC particles reinforcement. The chemical composition of the alloy used is given in Table 1. The amount of the reinforcement particles in the examined composite was 17.8% by volume while the average size of particles was $0.7\mu m$. The composite was subjected to two different heat treatments: T1 and T6 to compare the ways in which the heat treatment methods on change the strengthening of the material [3].

Table 1 Chemical composition of Al2124 alloy (mass fraction, %) [17].

<i>Cu</i>	<i>Mg</i>	<i>Mn</i>	<i>Ti</i>	<i>Zn</i>	<i>Cr</i>	<i>Fe</i>	<i>Si</i>	<i>Al</i>
4.18	1.46	0.52	0.15	0.25	0.1	0.3	0.2	balance

The composite after the T1 heat treatment was its *soft* version. It was annealed at $491^\circ C$ for 6h, cooled in the air in normal conditions and naturally aged to a substantially stable condition [3].

The *hard* material, was subjected to T6 heat treatment, i.e. it was solution treated at $491^\circ C$ for 6h and then water quenched and artificially aged for 4h at $191^\circ C$. As a result of this treatment the Cu-Al-Mg precipitates appeared. After the solution heat treatment, the material was rapidly cooled to obtain solid solution supersaturated by alloying elements. The last step was the aging process, in which the dispersed particles precipitate from the supersaturated solution. For the purposes of comparison, the *in situ* diffraction was performed during tensile test for the pure 2124 aluminum alloy specimen after the same type of heat treatment (T6) [3].

The main difference between T1 and T6 material variants is the appearance of different types and sizes of precipitations. As a result of the T1 treatment, the thermodynamically stable, relatively large S-phase particles with chemically incoherent Al_2CuMg are formed. On the other hand, the T6 treatment leads to the emergence of small metastable semi-coherent S particles. This phenomenon is typical for 2X24 aluminum alloys in which the mass ratio of Cu to Mg varies from 2.1 to 4 [17]. The above mentioned precipitations are considered as to cause locking dislocations disabling slipping on crystallographic planes and hindering plastic process in the material when tensile forces are applied. The input of this mechanism, i.e. precipitation hardening, into the material hardening has been investigated in this work [3].

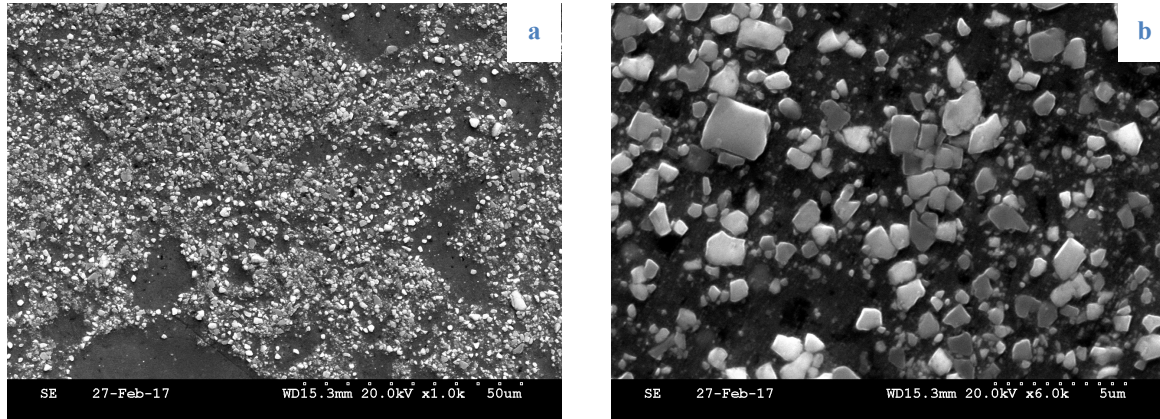


Fig. 1 The SEM images of Al/SiCT6 composite. SiC particles are shown with white contrast. The magnifications used for depicting were 1000 times in a) and 6000 times in b) [3].

In Fig. 1, the SEM pictures of *hard* specimen (Al/SiCT6) are presented, for different magnifications. The first observation is that the reinforcement particles are not distributed perfectly homogenously. On the other hand, in some approximation, the uniform particles' distribution can be presumed. It is worth mentioning that some dispersion of the particles size can be observed (although the nominal particle size is $0.7\mu m$).

The pole figures of both phases in Al/SiC material were measured with the Panalytical Empyrean diffractometer with a Cu X-ray tube for which radiation wavelengths were: $K_{\alpha_1} = 1.54056\text{\AA}$, $K_{\alpha_2} = 1.54439\text{\AA}$. Because the texture is insignificant random ODFs were assumed for *Al* and *SiC*.

The setup of diffraction measurements

The diffraction experiments with the neutron radiation were performed at the Frank Laboratory of Neutron Physics, Joint Institute for Nuclear Research in Dubna (Russia) on the EPSILON MDS diffractometer designed for stress/strain measurements.

The experiment was performed with the Time-Of-Flight (TOF) method which is a type of energy dispersive method. The neutrons' beam applied was polychromatic, i.e. formed by the neutrons of different energies. This method allows applying Bragg's law to different lattice planes at a fixed scattering angle, typically $\theta = 90^\circ$. The concept of this method involves measuring the time of flight of the neutrons over a given distance instead of measuring the diffraction angle [3]. The calculations of the interplanar spacings for given *hkl*s are based on the combination of the de Broglie equation and Bragg's law:

$$d_{hkl} = \frac{ht}{2\sin\theta m_n L} \quad \text{eq. 12}$$

where:

$m_n = 1.675 \cdot 10^{-27} kg$ - is the neutron mass,

$h = 6.63 \cdot 10^{-34} J \cdot s$ - Planc's constant,

t - time of flight of the neutron from its source to the detector,

θ – Bragg's angle,

L – the total distance between the neutron source and the detector; for EPSILON-MDS it is 107.03m.

After a substitution into this equation all known values, including parameters characterizing the unique instrumentation in JINR in Dubna, the interplanar distance turns out to be dependent only on the time of flight of the neutrons (t):

$$d = 1.849 \cdot t [nm] \quad \text{eq. 13}$$

The conclusion is that the time of flight of the neutrons can be directly used for the measurement of interplanar spacings in the specimen examined [3].

The specimen geometry, the measurement setup and the specimen pictures are presented in Fig. 2a-d. The measured gauge length was 15mm and its cross section was 4.4mm×4.4mm. The specimens were fixed in a tensile machine, located in the goniometer and subjected to the tensile test until fracture. The experiments were executed during the course of in situ tensile test whose objective was to measure d_{hkl} and resulting strains and stresses for different stages of macrostrain. To achieve these goals the diffraction measurements were performed for a few stages of the specimen deformation: in case of the *hard* specimen it was 6 stages while in case of *soft* one it was 9 stages. The residual state of both specimens was measured for the initial state of specimens and after they fractured. The *in situ* tensile test (8 stages of deformation, initial and residual state) was also performed for the specimen prepared from the material used as a matrix in the Al/SiC composite i.e. Al2124T6 alloy [3].

The data resulting from the experiments were gathered with two detectors' sets in order to measure lattice strains in two directions: in direction of the force applied, parallel to the axis of the specimen, and in the perpendicular direction (see detectors 2 and 8 in Fig. 2b, for which the diffraction angle was $2\theta = 90^\circ$). The values of interplanar spacings d_{hkl} were measured simultaneously for different hkl reflections. As showed in the exemplary diffractogram d_{hkl} values ranged between 0.8 - 2.7Å. It covered reflections from both phases of Al/SiC composite (Fig. 3). The incident beam was 10mm wide and the time of one exposure was 22 - 23 hours for every specimen and every stage of its deformation [3].

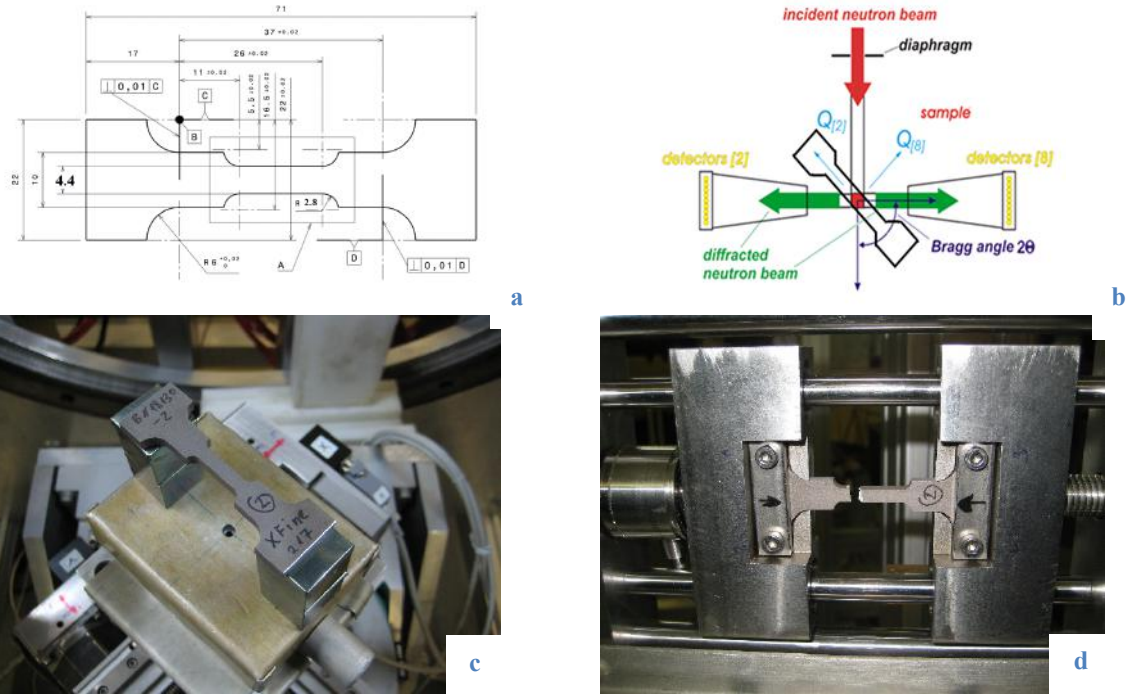


Fig. 2 Dimensions of Al/SiC specimen: a), the geometry of the experiment b), Al/SiC specimens: c) before experiment, d) after fracture in the tensile machine [3].

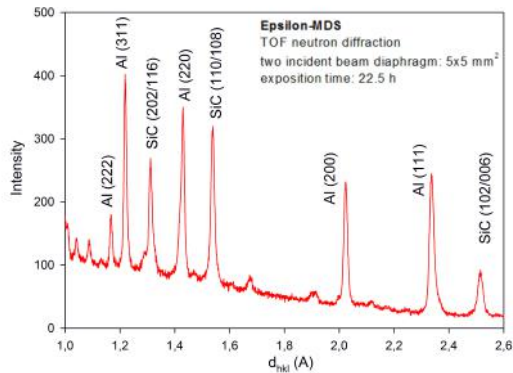


Fig. 3 The diffractogram obtained for Al/SiC composite on EPSILON diffractometer [3].

Results analysis

In the *in situ* tensile tests the relative lattice strains in the direction of the load $\langle \varepsilon_{11} \rangle_{\{hkl\}}$ and in the transverse direction $\langle \varepsilon_{22} \rangle_{\{hkl\}}$ were determined using eq. 14 [3]:

$$\langle \varepsilon_{11} \rangle_{\{hkl\}} = \frac{\langle d_{LD} \rangle_{\{hkl\}}^{\Sigma} - \langle d_{LD} \rangle_{\{hkl\}}^0}{\langle d_{LD} \rangle_{\{hkl\}}^0} \quad \text{and} \quad \text{eq. 14}$$

$$\langle \varepsilon_{22} \rangle_{\{hkl\}} = \frac{\langle d_{TD} \rangle_{\{hkl\}}^{\Sigma} - \langle d_{TD} \rangle_{\{hkl\}}^0}{\langle d_{TD} \rangle_{\{hkl\}}^0}$$

where: $\langle d \rangle_{\{hkl\}}^{\Sigma}$ and $\langle d \rangle_{\{hkl\}}^0$ are the interplanar spacings measured for a loaded (for a given applied stress Σ_{11}) and non-loaded sample (initial, i.e. for $\Sigma_{11} = 0$) with the $\langle \dots \rangle_{\{hkl\}}$ brackets denoting an average over the diffracting grains volume for a given reflection hkl . Indices LD and TD mean that the interplanar spacings were measured in the direction of the load and in the transverse direction, respectively. This methodology allowed obtaining the

changes of lattice strains (eq. 14) for separate phases and for different hkl 's reflections (in both phases) after determining the position of peaks for every stage of the sample deformation. Next, the values of strains in a given direction were used to calculate the stress values in both phases and for different hkl s. After using the weighted average, the mean macroscopic stress value could be obtained in relation to the macroscopic strain of the specimen.

The analysis and comparison of macrocurves for the hard state of Al2124 alloy and the Al/SiC composite (Fig. 4) allows to state that the significant role in the material hardening plays the addition of reinforcement to the composite. In both cases the same T6 thermal treatment was applied so the changes in composite macroscopic curve (comparing to the single phase alloy) can be explained by the addition of reinforcement particles. It can be observed that while the ultimate tensile strength of aluminum alloy is about $370MPa$, its value for the composite reaches much higher level of $650MPa$. Moreover it was found that the experimental macroscopic curves were confirmed by the calculations of self-consistent model predictions. It should be emphasized that model predictions were performed assuming the same value of CRSS as previously for Al2124 T6 alloy (the $\tau_{0Al} = 120MPa$ was chosen in this case) [3].

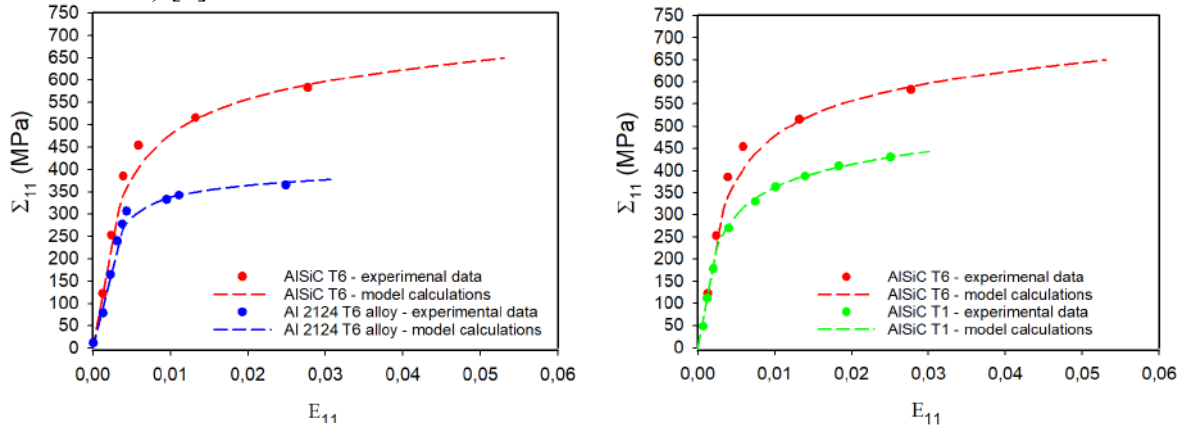


Fig. 4 Macroscopic dependence of macroscopic stress (after stabilization) vs. macroscopic strain for: a) single phase Al2124 T6 alloy and Al/SiC T6 composite (model predictions for T6 treatment: $\tau_{0Al} = 120MPa$ and $H_{Al} = 50MPa$), b) two types of composite after T1 and T6 heat treatment (model predictions for T1 treatment: $\tau_{0Al} = 82MPa$ and $H_{Al} = 50MPa$).

When comparing the experimental results for the composites after applying a different heat treatment, it can be seen that the yielding point for Al/SiC T1 and its ultimate tensile strength are obviously different than for Al/SiC in T6 – their values are about $200MPa$ and $450MPa$, respectively. As the reinforcement particles are the same in both types of the composite (17.8% of SiC particles with a size of $0.7\mu m$) the appearance of different macroscopic curves for this material can be caused only by the changes of the aluminum matrix microstructure due to a different thermal treatment. Indeed, in the case of the Al/SiC T1 material, the best fit of the model calculations was obtained for $\tau_{0Al} = 82MPa$, $H_{Al} = 50MPa$, i.e. the Al matrix is softer compared to the alloy after the T6 treatment. This effect can be explained by the size of precipitates (mainly Cu-Al-Mg) created during thermal treatments in the Al matrix. The T6 process (quenching and artificial ageing) leads to much smaller precipitates compared to these after T1 treatment (slow cooling and natural ageing). As mentioned above, the small size of precipitates (after the T6 treatment) leads to the precipitation hardening, while the strengthening effect is less significant for large precipitates (after the T1 treatment) [3].

Conclusions

Thanks to the methodology applied the hardening mechanisms and strengthening type could be observed, illustrated and characterized. The comparison of the results for Al/SiC and aluminum alloy samples subjected to the T6 treatment nearly the same plastic behavior was found for the aluminum phase. In this case, the overall stress was much higher in the case of composite, during whole tensile test. This type of increase in stress values is characteristic for composites and is due to the stress being localized in the reinforcement. This effect is well predicted by the model used. The second comparison was made for the Al/SiC composite subjected to different treatments: T1 and T6 to present the influence of heat treatment of different types on the hardening of the composite and to find the reason for this phenomenon. It was observed that stresses in the composite are higher for the material subjected to the T6 treatment. The Al-matrix is harder in this material, causing higher overall stress. This can be explained by a smaller size of precipitates in the Al matrix after the T6 process (quenching and artificial ageing) leading to locking dislocations and important hardening during the plastic deformation. Comparison of the elastoplastic self-consistent model with measured lattice strains allowed to find out the micro-mechanical properties of the 2124 aluminum alloy and the Al/SiC composite, i.e. critical resolved shear stress and hardening parameter for aluminum for both heat treatments. By using theoretical calculations and diffraction results, the roles of the matrix and reinforcement in composite hardening were described.

References

- [1] A. Baczański, "Stress fields in polycrystalline materials studied using diffraction and self-consistent modeling," postdoctoral dissertation, AGH - University of Science and Technology, Kraków, 2005.
- [2] A. Baczański and C. Braham, "Elastoplastic properties of duplex steel determined using neutron diffraction and self-consistent model," *Acta Materialia*, vol. 52, no. 5, pp. 1133–1142, Mar. 2004.
- [3] E. Gadalińska, "Micromechanical properties and stresses in two-phase polycrystalline materials studied using diffraction and self-consistent model," Doctoral Thesis, AGH - University of Science and Technology, Kraków, 2018.
- [4] A. Maciejny, "Mechanizm umocnienia kompozytów," *Krzepnięcie metali i stopów. Krystalizacja i własności kompozytów odlewanych.*, vol. 7, pp. 335–353, 1984.
- [5] R. J. McElroy and Z. C. Szkoziak, "Dislocation–Substructure–Strengthening and Mechanical–Thermal Treatment of Metals," *International Metallurgical Reviews*, vol. 17, no. 1, pp. 175–202, Jan. 1972.
- [6] M. Rozmus-Górniewska, "Umocnienie wydzieleniowe stopu Al z Cu +umocnienie stali," Kraków.
- [7] T. W. Clyne and P. J. Withers, *An Introduction to Metal Matrix Composites*. Cambridge University Press, 1993.
- [8] R. J. Arsenault and N. Shi, "Dislocation generation due to differences between the coefficients of thermal expansion," *Materials Science and Engineering*, vol. 81, pp. 175–187, Aug. 1986.
- [9] R. J. Arsenault, L. Wang, and C. R. Feng, "Strengthening of composites due to microstructural changes in the matrix," *Acta Metallurgica et Materialia*, vol. 39, no. 1, pp. 47–57, Jan. 1991.
- [10] S. B. Prabu, L. Karunamoorthy, S. Kathiresan, and B. Mohan, "Influence of stirring speed and stirring time on distribution of particles in cast metal matrix composite," *Journal of Materials Processing Technology*, vol. 171, no. 2, pp. 268–273, Jan. 2006.
- [11] K. Suryanarayanan, R. Praveen, and S. Raghuraman, "Silicon carbide reinforced aluminium metal matrix composites for aerospace applications: a literature review,"

International Journal of Innovative Research in Science, Engineering and Technology, vol. 2, no. 11, pp. 6336–6344, 2013.

- [12] S. H. Avner, *Introduction to physical metallurgy*. New York: McGraw-Hill, 1964.
- [13] Y. Lakhtin and N. Weinstein, *Engineering physical metallurgy*. University Press of the Pacific, 2000.
- [14] M. M. Boopathi, K. P. Arulshri, and N. Iyandurai, “Evaluation of mechanical properties of aluminium alloy 2024 reinforced with silicon carbide and fly ash hybrid metal matrix composites,” *American Journal of Applied Sciences*, vol. 10, no. 3, pp. 219–229, 2013.
- [15] S. V. S. Narayana Murty, B. Nageswara Rao, and B. P. Kashyap, “On the hot working characteristics of 6061Al–SiC and 6061–Al₂O₃ particulate reinforced metal matrix composites,” *Composites Science and Technology*, vol. 63, no. 1, pp. 119–135, Jan. 2003.
- [16] M. E. Fitzpatrick, “A study of the effects of a quench residual stress field on fatigue in an Al/SiCp metal matrix composite,” University of Cambridge, 1995.
- [17] F. Xu, J. Zhang, Y. Deng, and X. Zhang, “Precipitation orientation effect of 2124 aluminum alloy in creep aging,” *Transactions of Nonferrous Metals Society of China*, vol. 24, no. 7, pp. 2067–2071, Jul. 2014.

Calibration of the Ductile Failure Criterion for Nickel-Based Superalloys Taking into Account the Localization of the Strain

Introduction

There are many ductile failure criteria allowing the modeling of failure of ductile materials such as metal alloys. The most frequently used one is the constant equivalent plastic strain criterion. According to this criterion, fracture occurs in a material when the equivalent plastic strain reaches a critical value:

$$\bar{\epsilon}^p = \bar{\epsilon}_f^p \quad (1)$$

where

$\bar{\epsilon}_f^p$ - accumulated equivalent plastic strain corresponding to material failure

$\bar{\epsilon}^p$ - equivalent plastic strain

This criterion, however simple and easy to use, was not confirmed by experiments. The classic experiment by von Karman [1] showed that marble and sandstone exhibiting brittle fracture under simple, uniaxial compression (no plastic strain before failure can be observed) could achieve significant plastic deformation when subjected to high hydrostatic pressure. This experimental observation led to the modification of the ductile failure criterion (1). A number of modified criteria, relating accumulated failure strain to stress state were formulated. One of them, used by many researchers was proposed by Johnson and Cook [2]. If the strain rate and temperature are constant, the strain to fracture is a monotonic function of the stress triaxiality, as shown in the equation bellow:

$$\bar{\epsilon}_f = C_1 + C_2 \exp(C_3 \eta) \quad (2)$$

where η (stress triaxiality parameter) is a ratio of the mean stress to equivalent stress

$$\eta = \frac{\sigma_m}{\bar{\sigma}} \quad (3)$$

This criterion (2) was further modified [3,4] to better fit experimental data. A good review of the ductile failure models was given in paper [5].

Another approach, typically used in the case of brittle fracture, is the stress approach. One of the most popular from this group is the maximum shear (MS) stress criterion. From this criterion, it follows that fracture may occur on a plane where the shear stress is maximum. In view of this fact, fracture is governed by the condition:

$$\tau_{\max} = (\tau_{\max}) \text{ and } \sigma_1, \sigma_2, \sigma_3 \quad (4)$$

where

$$\tau_{\max} = \max \left\{ \frac{\sigma_1 - \sigma_2}{2}, \frac{\sigma_2 - \sigma_3}{2}, \frac{\sigma_3 - \sigma_1}{2} \right\} \quad (5)$$

In the case of metal alloys exhibiting elastic - plastic behavior, ductile failure can be expected for most stress states. In this case, we should use the strain approach (ductile failure criterion). Determining failure strain (equivalent plastic strain) using static tension we should remember about the fact, that elongation calculated according to standard [6], [7], [8] and [9] is an average value of deformation of the specimen gage part, and that strain localization occurrence leads to formation non-uniform stress and strain distribution in the cohesive zone (neck). The present paper is concerned with error which can appear when we estimate the critical (corresponding to failure) value of equivalent plastic strain using static tensile tests while disregarding the localization of strain.

Material and experimental technique

The material used for the tests was nickel alloy. Nickel alloys are characterized by high mechanical properties and corrosion resistance at elevated temperatures. For these reasons, they are widely used in the aviation and nuclear industries, especially in gas turbines, jet engines and other components working in extreme conditions. For our tests, we used two different alloys. One was INCONEL 718, which is characterized by high ductility. The other was nickel alloy in the form of the cast, which is very brittle and exhibits low ductility. Table 1 shows the chemical compositions of INCONEL 718. The chemical composition of the other alloy is not permitted to be published .

Table 1. Chemical composition [% weight] – INCONEL 718

C	Mn	P	S	Si	Cr	Ni	Al
0,03	0,08	0,01	0,0005	0,09	18,49	52,92	0,6
Mo	Cu	Nb	Ta	Ti	Co	B	Fe
2,88	0,04	5,12	0,01	0,86	0,27	0,004	18,39

The tensile tests were carried out according to ASTM E8/E8M-16a and ASTM E21-09. 21 and 138 specimens were tested for INCONEL 718 and nickel alloy (cast), respectively. Table 2 shows more details regarding the testing program. For all tensile tests, specimens designed according to the ASTM E8M-16a requirements were used. The drawing of the specimen is shown in Fig. 1.

Table 2. Test plan for two nickel alloys

INCONEL 718		Nickel alloy - cast	
Temperatures of the tests [F]	Number of tested specimens	Temperatures of the tests [F]	Number of tested specimens
75	12	75	16
400	1	1022	16
750	6	1202	16
1100	1	1292	16
1300	1	1382	16
		1472	16
		1562	16
		1652	16
		1742	10

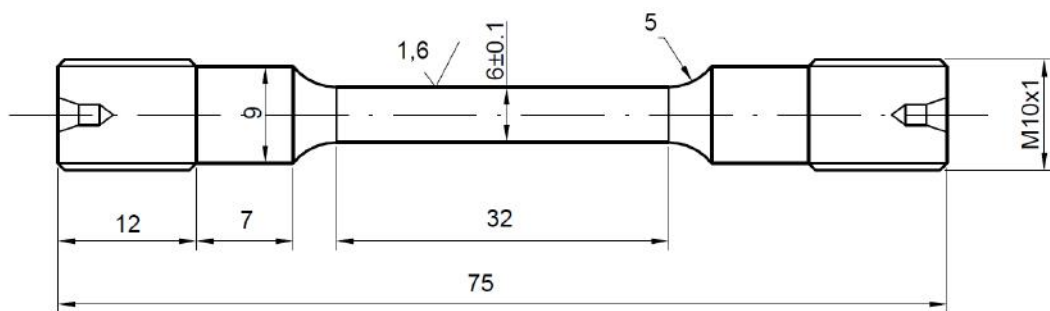


Fig. 1. Specimen used in tensile tests (according ASTM E8M-16a).

For tensile tests, the servo hydraulic machines MTS 318.10 with load capacity ± 100 kN were used. The machine (Fig. 2) was equipped with the furnace (INSTRON SFL mod 3812K control system) with three heating zones and an extensometer MTS mod 63253F-14. During the tests, temperature was measured using three type S thermocouples connected with the control system and furnace.



Fig. 2. Testing machines

The tensile tests were carried out according to the ASTM and ISO standards. For all specimens, standard elongation (according to the ASTM E8/E8M-16a and PN-EN ISO 6892-1:2016-09) was calculated. Standard elongation for specimens with the gauge length equal five times the diameter was marked as $El(A5)$.

During the tensile test, the specimen's gauge part is initially deformed in the elastic regime. After reaching the yield limit, plastic deformation starts to develop in the gauge part of the specimen. The test specimen is strained uniformly along its gauge part length up to the point of maximum force. This means that the gauge section gets longer and thinner but keeps its cylindrical shape. As soon as the maximum force is reached a neck begins to form in the gauge part of the specimen. All further plastic deformation develops only at the neck since strain hardening cannot compensate the reduction of the neck cross-section area any more. This fact has important consequences. When calculating the final equivalent plastic strain $\bar{\epsilon}_f^p$ corresponding to material failure it is necessary to take into account the strain localization. In order to estimate correctly this value, we have to take into account a reduction of the area, which is more pronounced for alloys with high ductility (Figure 3b), but hardly detectable for brittle alloys (Figure 3c).

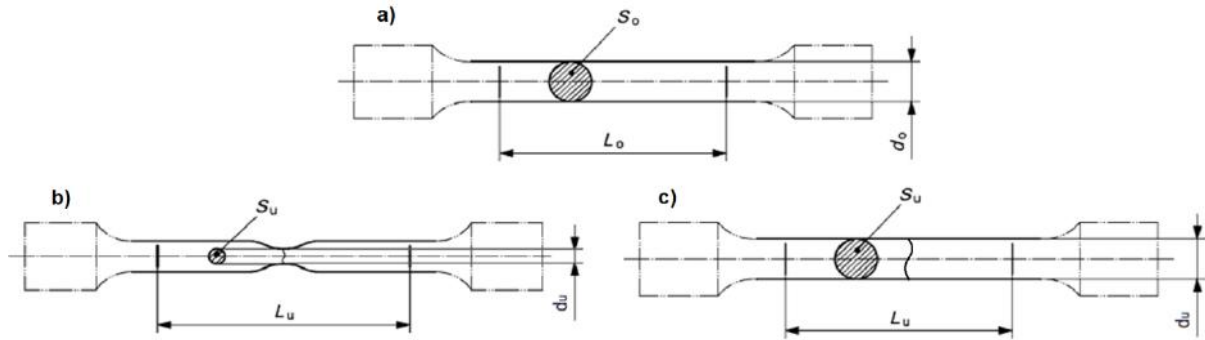


Fig. 3. Shape of the specimens: a) before tensile test, b) after tensile tests for ductile alloy, c) after tensile tests for brittle alloy

For all specimens, final equivalent plastic strain $\bar{\epsilon}_f^p$ was calculated for the smallest cross-section of the neck. Transversal plastic strain for this cross-section was calculated using measurements of the specimen's diameter before and after the test. Assuming plastic isotropy and incompressibility of the material, two other principal plastic strains were calculated using the simple formula:

$$\epsilon_y^p = \epsilon_z^p = -\frac{1}{2} \epsilon_x^p \quad (6)$$

The equivalent plastic strain is the function of three principal strains (ϵ_x , ϵ_y , ϵ_z) as defined below:

$$\epsilon^p = \frac{\sqrt{2}}{3} \sqrt{(\epsilon_x^p - \epsilon_y^p)^2 + (\epsilon_y^p - \epsilon_z^p)^2 + (\epsilon_z^p - \epsilon_x^p)^2} \quad (7)$$

Taking into account relation (6) we can calculate the final equivalent strain using following formula:

$$\epsilon^p = \frac{\sqrt{2}}{3} \sqrt{(-2\epsilon_y^p - \epsilon_y^p)^2 + (\epsilon_y^p - \epsilon_y^p)^2 + (\epsilon_y^p + 2\epsilon_y^p)^2} = 2\epsilon_y^p \quad (8)$$

It is worth to note that the equivalent plastic strain in the case of simple tension has the value equal to the value of axial strain in the direction of the force. The value of standard elongation $El(A5)$ was calculated according to the ASTM E8/E8M-16a standard. According the ASTM standard, gauge lengths markings of the test specimens were made before tensile tests. After tensile tests, two halves of specimens fractures were fit together and the distance between the gage part was measured. In order to calculate elongation, the following formula was used:

$$El(A5) = \frac{\Delta L}{L_0} = \frac{L - L_0}{L_0}. \quad (9)$$

Results and discussion

Standard elongation $El(A5)$ and the final equivalent plastic strain $\bar{\epsilon}_f^p$ are plotted as the function of test temperature in Figure 4, for nickel cast alloy. This alloy is characterized by low ductility, especially at room temperature. For these specimens, the fracture is brittle so the neck does not appear. Only at higher temperatures the ductility is higher and we can observe the formation of a neck.

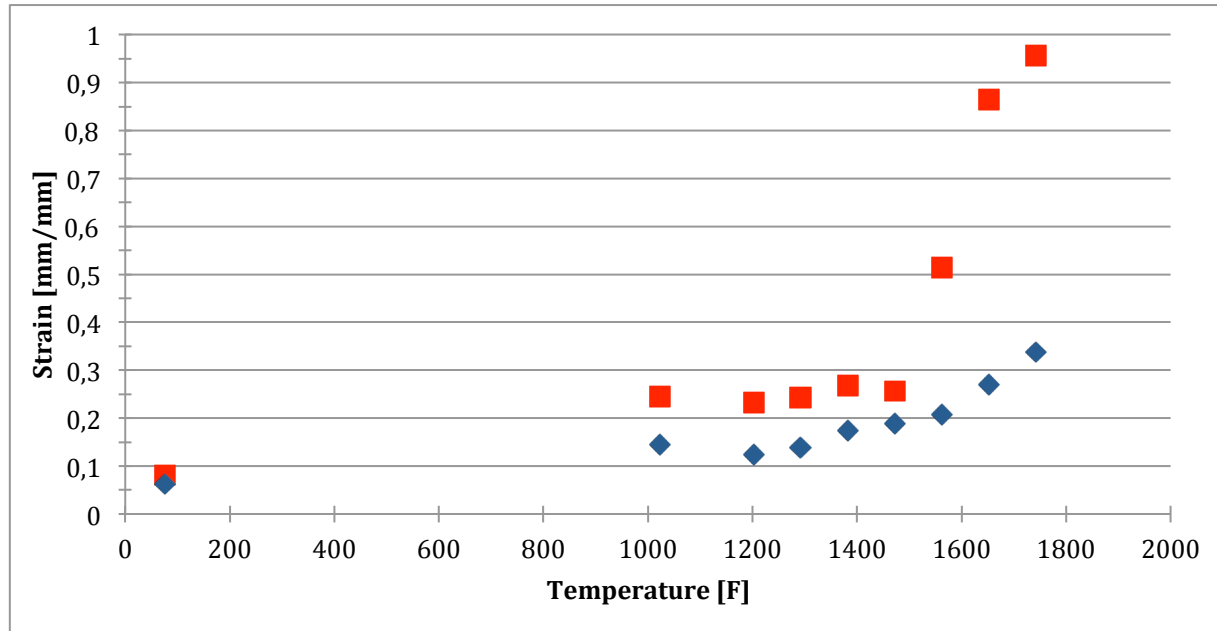


Fig. 4. Final equivalent plastic strain ($\bar{\epsilon}_f^p$) – marked red, and standardized elongation ($El(A5)$) – marked blue, for nickel alloy (cast).

The error of failure strain estimation for all temperatures is shown in Figure 5. It was calculated according to the formula bellow:

$$\left(\frac{\bar{\epsilon}_f^p - El(A5)}{El(A5)} \right) \times 100\% \quad (10)$$

where:

$\bar{\epsilon}_f^p$ - final equivalent plastic strain calculated according to formula (8),

$El(A5)$ - standard elongation of the specimen's gage part.

If we compare the standard elongation ($El(A5)$) and final equivalent plastic strain ($\bar{\epsilon}_f^p$), we can notice that the higher the temperature is the higher the error is. This is associated with the ductility of the alloy in question increasing with the temperature. At higher temperatures, the reduction of area is more visible. If we do not take into account the reduction of the area at high temperatures, we will receive huge error of failure strain estimation.

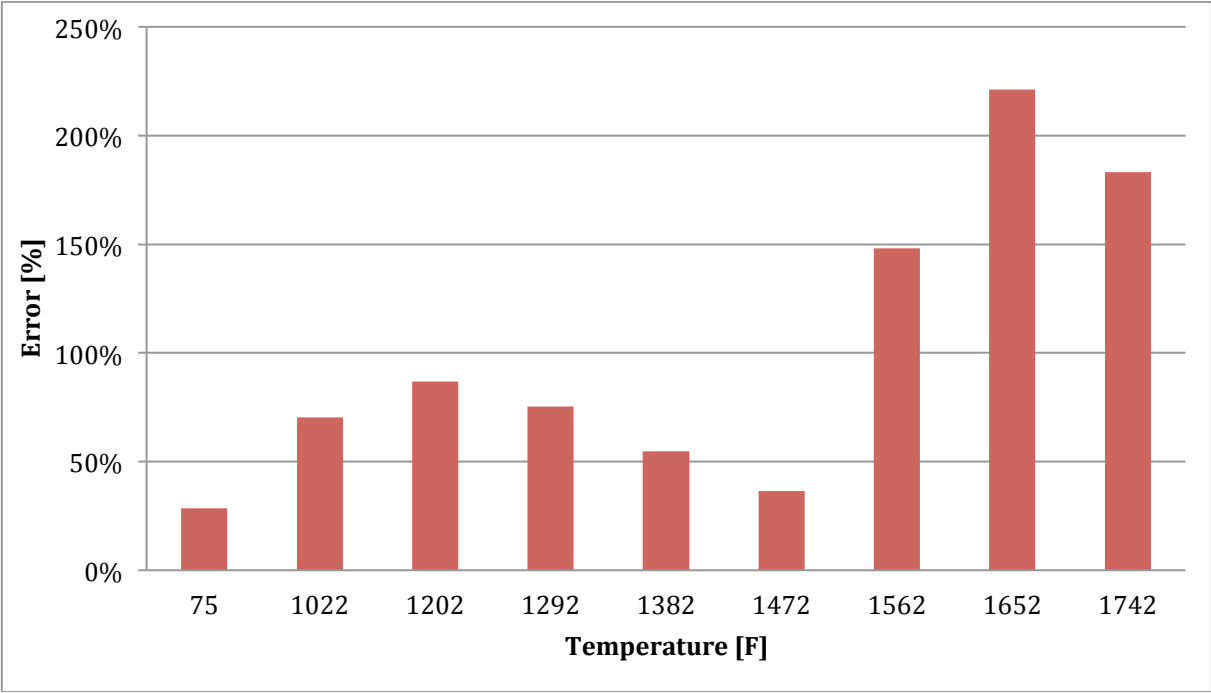


Fig. 5. Error calculated according to formula (10) for nickel alloy (cast).

The second alloy tested was INCONEL 718. The results for this alloy are presented in Figure 6. This alloy is characterized by high ductility so during tests a typical neck appears in the gage part of the specimen.

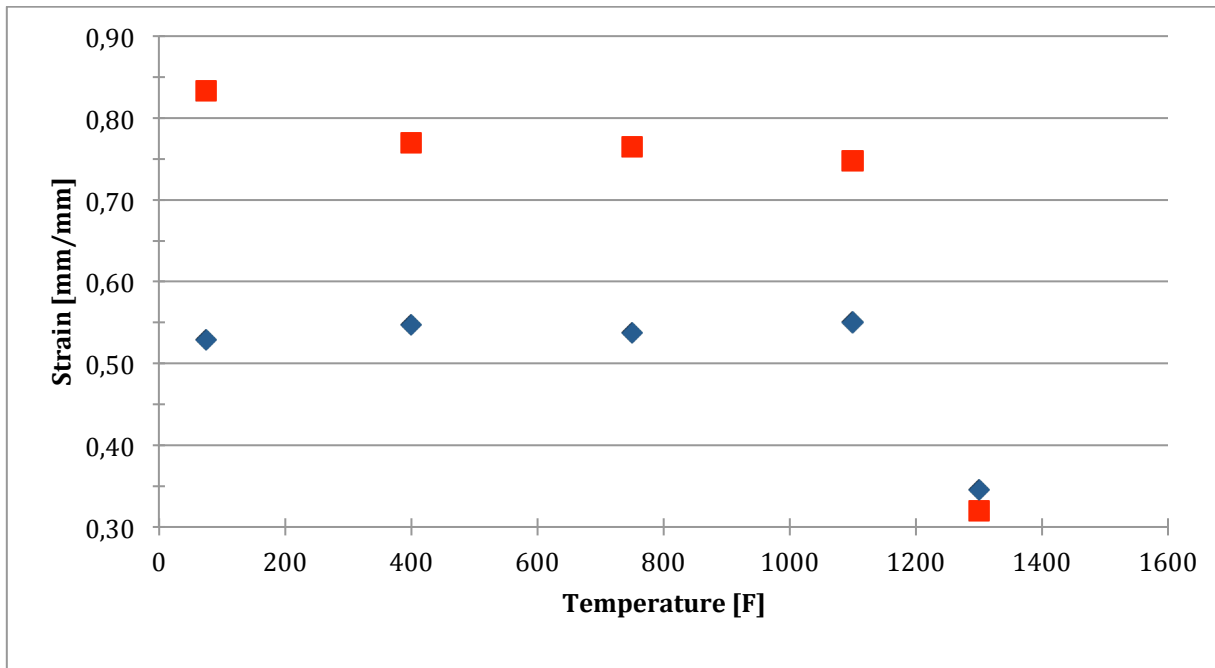


Fig. 6. Equivalent plastic strain ($\bar{\epsilon}_f^p$) - marked red, and standard elongation ($El(A5)$) – marked blue, for nickel alloy for INCONEL 718.

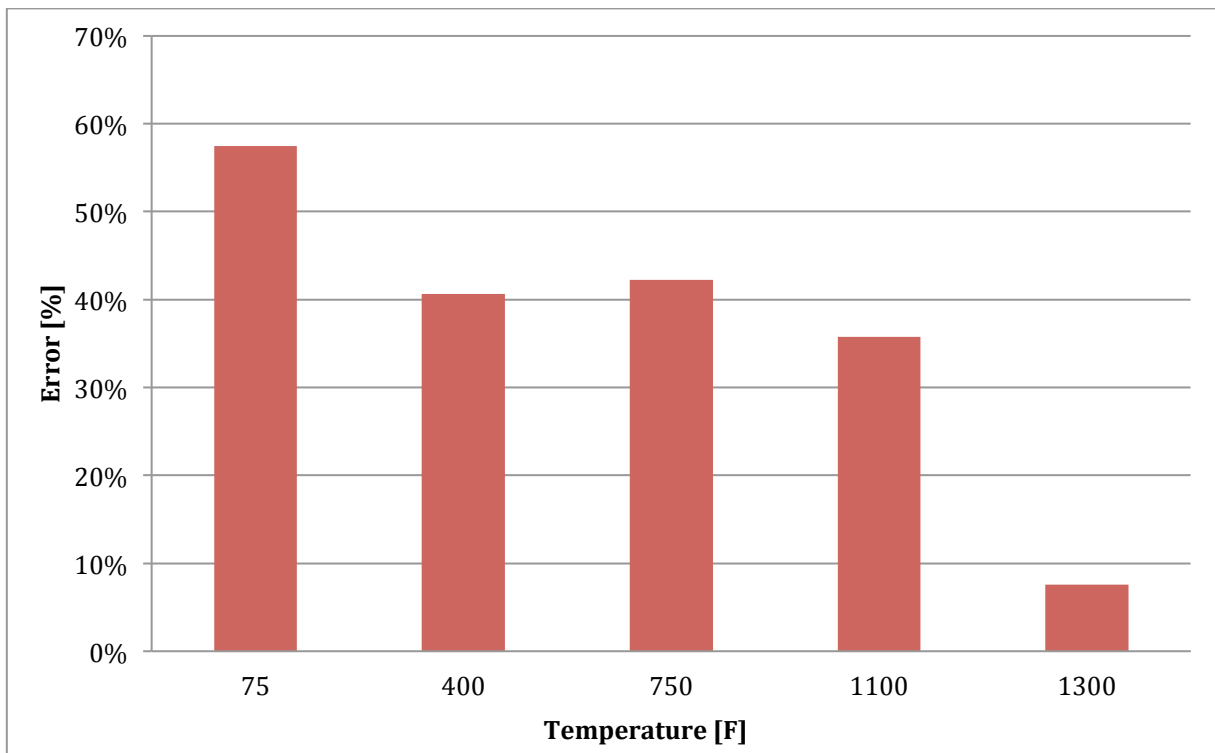


Fig. 7. Error calculated according to formula (10) for INCONEL 718.

In this case, at high temperatures a smaller error of failure strain estimation was obtained as it can be seen in Figure 7. This can be attributed to the ductility decreasing with the rising temperature. If the neck does not appear, as in the case of the test at 1300F, the reduction of the cross section in the whole gage section is almost the same – see Figure 8b.

The error in this case is negligible. At room temperature (Figure 8a), strain localization in the form of the neck is clearly visible.



a) room temperature



b) 1300 F

Fig.8 Fracture appearance for: (a) room temperature and (b) temperature 1300F for INCONEL 718 alloy

Calculation of final equivalent plastic strain using standard static tension test results

As it was proved above, standard elongation $El(A5)$ calculated according to standards [6], [7], [8] and [9] should not be used as the value of final equivalent plastic strain in failure condition (1). However, we can calculate the value of the final equivalent plastic strain based on the properly determined results of static tension test. To do this we have to use reduction of the area (RoA), which is calculated according to the standards using the formula below:

$$RoA = \frac{A_0 - A_u}{A_0} \cdot 100\% \quad (11)$$

where A_0 stands for the initial value of the cross-section area and A_u stands for the final value of the area of the smallest cross-section of the gage part of the specimen. Having measured the smallest diameter of the gage part of the specimen before (d_0) and after (d_u) test we can write:

$$RoA = \frac{d_0^2 - d_u^2}{d_0^2} \cdot 100\% = \left(1 - \left(\frac{d_u}{d_0} \right)^2 \right) \cdot 100\% \quad (12)$$

To calculate transversal strain using the given reduction of the area, we have to use the following relation:

$$\varepsilon_y^p = \frac{d_0 - d_u}{d_0} = 1 - \frac{d_u}{d_0} \quad (13)$$

and substituting d_u/d_0 calculated from relation (12)

$$\varepsilon_y^p = 1 - \sqrt{1 - \frac{RoA}{100\%}} \quad (14)$$

Finally, using equation (8) we can calculate final equivalent plastic strain using the following relation:

$$\bar{\varepsilon}_f^p = 2 \cdot \left(1 - \sqrt{1 - \frac{RoA}{100\%}} \right) \quad (15)$$

Conclusions

This study led to the following conclusions:

1. When using the results of tensile tests for modeling of material failure it is very important to calculate final equivalent plastic strain properly. The standard elongation cannot be used as the maximum strain the material can reach. Use this simplification will result in large errors of the material ductile failure numerical simulations.
2. The source of this error results from ignoring the localization of the strain (appearance of a neck) in the final phase of the tensile test.
3. For cast alloy, the error increases with increasing ductility of the alloy caused by the temperature rise. For the investigated alloys, the error reached 100%. For standard INCONEL 718 alloy, we can observe the opposite trend: the error decreases with the rise of the temperature due to decreasing ductility.

References

- [1] von Karman Th, Festigkeitversuche unter allseitigem Druck, *Z. des Ver. Deutsch Ingenieurie*, 55 (1911), pp. 1794 – 1757.
- [2] Johnson GR, Cook WH., Fracture characteristics of three metals subjected to various strains, strain rates, temperatures and pressures. *Engineering Fracture Mechanics* (1985);21(1):31–48.
- [3] Cockcroft MG, Latham DJ. Ductility and the workability of metals. *Journal of the Institute of Metals*, (1968) ;96:33–9.
- [4] Wilkins ML, Streit RD, Reaugh JE. Cumulative-strain-damage model of ductile fracture: simulation and prediction of engineering fracture tests. Technical Report UCRL-53058, Lawrence Livermore National Laboratory; October 1980.
- [5] Tomasz Wierzbicki, Yingbin Bao, Young-Woong Lee, Yuanli Bai. Calibration and evaluation of seven fracture models, Impact and Crash worthiness Laboratory, Massachusetts Institute of Technology.
- [6] PN-EN ISO 6892-1:2016-09 - Metale -- Próba rozciągania -- Część 1: Metoda badania w temperaturze pokojowej.
- [7] PN-EN ISO 6892-2:2011 - Metale -- Próba rozciągania -- Część 2: Metoda badania w podwyższonej temperaturze.

[8] ASTM E8/E8M - 16A - Standard Test Methods for Tension Testing of Metallic Materials.

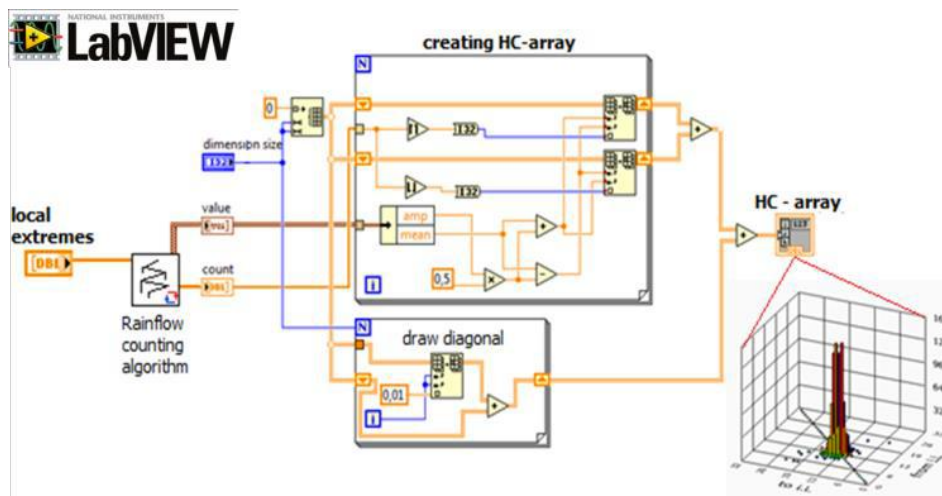
[9] ASTM E21 – 09 - Standard Test Methods for Elevated Temperature Tension Tests of Metallic Materials.

OTHER WORKS

Study of Load Spectrum occurring in the course of photogrammetric missions of the UAV

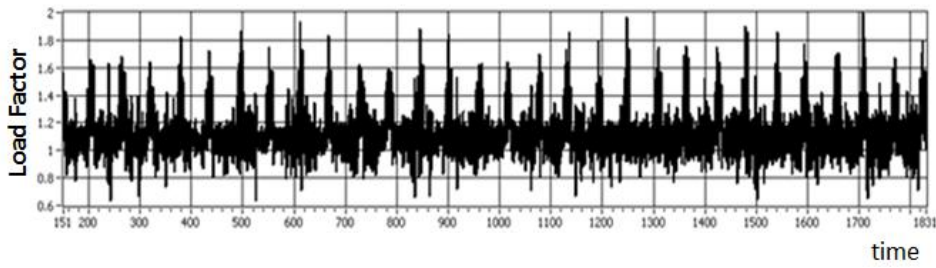
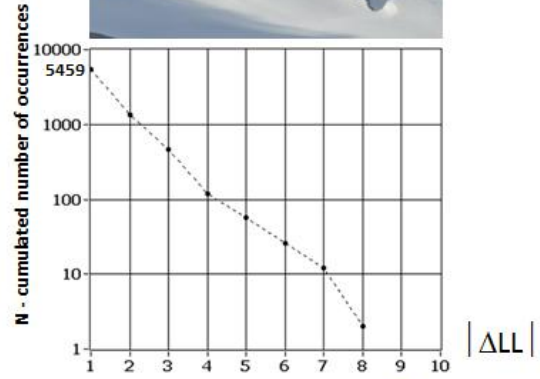
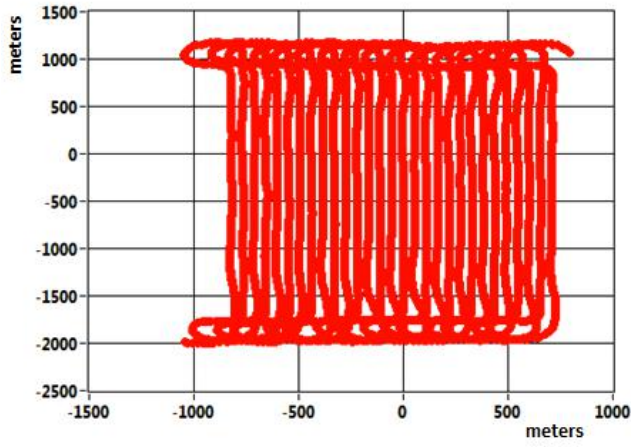
One of common applications of light-weight civilian UAVs are aerial monitoring and photogrammetry.

A good example of such an application is MONICA Project, which was devoted to aerial monitoring and photogrammetry of Antarctic Specially Protected Areas (ASPA) in King George Island (KGI). As a UAV platform there was used the PW-ZOOM, a plane powered by 4,8 hp gas engine, having 3,2 m of wingspan and 24 kg of take-off weight. During three Antarctic spring seasons (2014-2016) the PW-ZOOM performed over KGI 33 flights of total distance 3641 km, and spent in the air 35,6 hours. Besides delivering a large amount of photogrammetry data, there were collected also flight-logs containing several parameters, which allowed for studying various flight dynamic aspects. The work involves the analysis of flight-logs, which is oriented towards investigation of load spectrum during photogrammetry missions. There were chosen some flights having the same scenario and flight-paths, but which were performed in different weather conditions, especially at different wind speeds. The load spectra were developed as half-cycle arrays of load factor signal (i.e. transfer arrays based on the rain flow counting algorithm – Fig. 1), and as incremental load spectra (Fig. 2). Calculation algorithms were prepared by the authors in the LabVIEW environment. The results obtained allow for assessing the influence of weather on the fatigue loads during flight. They can be useful for preparing the bases necessary for load spectrum extrapolation and preparation of the fatigue tests of PW-ZOOM structure or similar planes.



Half-cycle array (i.e. rain flow matrix) derivation algorithm

Chosen part of photogrammetry track -
 (Flight PW-ZOOM 2014_11-27)
 Total length of analyzed track: 101,9 km

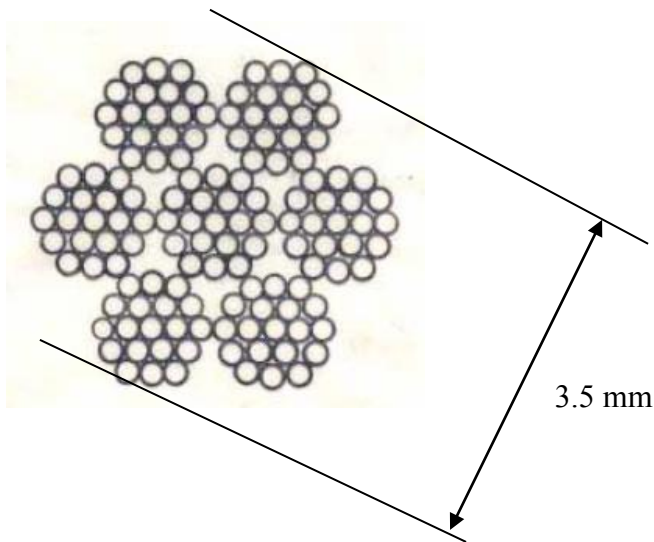


The Load Spectrum
 obtained for
 analyzed
 flight

Example of flight track and load signal and derived load spectrum.

The Fatigue Life of Cables in Aircraft Flight Control Systems

Aviation cables for flight control systems are made from carbon steel wires or stainless steel wires. Wires are of small diameter and high tensile strength. For example, cables made from zinc coated carbon steel according to the Russian standard TU 14-4-1266-83, are used in the PZL M28 aircraft. The cable is made from 7 strands. Each strand contains 19 wires of diameter $0.22 \div 0.30$ mm (in total: 133 wires) of minimum tensile strength 2160 MPa. The nominal wires cross-section is 5.447 sq.mm, and minimum-breaking force is 8600 N.



Cross-section of aviation cable KSAN 3,5 according to standard TU 14-4-1266-83

According to the standard TU 14-4-1266-83, the positive result of endurance test of the KSAN 3,5 cable is when breaking force after the test is at least 65% of the nominal force and the number of broken wires is not greater than 14% of 133 wires (18 wires).

In the year 2007, maintenance inspection of PZL M28 family airplanes operated by the Polish Air Force revealed an increased number of broken wires in the KSAN 3,5 cables in the elevator and rudder control systems – see Fig. 2. In some cases, the number of broken wires was greater than 8, which is maximum allowable number.



The damaged cable KSAN 3,5 removed from the aircraft

In response to this occurrence, the actions were undertaken by PZL MIELEC as the aircraft producer:

- checking of chemical composition and tensile strength of damaged cables,
- identifying the supplier of these cables,
- inspecting cables in control systems in other M28 airplanes,
- performing endurance tests of the KSAN 3,5 cables.

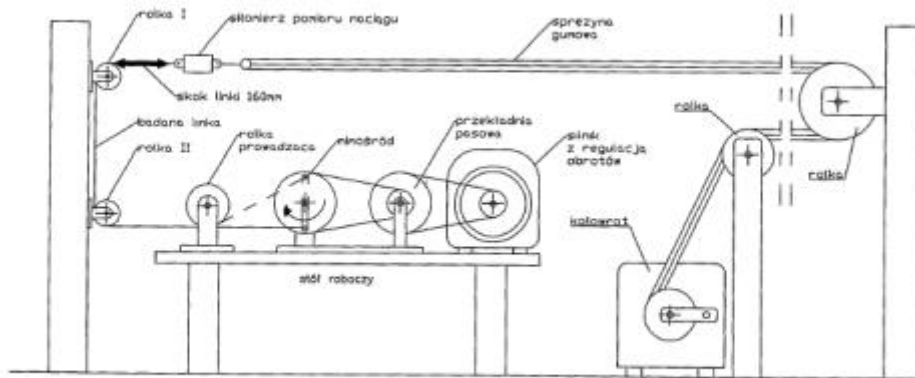
The chemical composition of the cable wires investigated was typical of carbon steel of grades 80, 85 and 65 (Russian), i.e. with 0.8%, 0.85% and 0.65% of carbon respectively, typical of the KSAN 3,5 cables. Also, the breaking force during the tests was above the minimum – see table below.

	Chemical compound			Breaking force
	C	Mn	Si	N
Specimen #1	0.85%	0.48%	0.24%	9.8 kN 9.7 kN
Specimen #2	-	-	-	9.4 kN 9.4 kN
Specimen #3	0.80%	0.50%	0.32%	9.2 kN 9.0 kN
Specimen #4	0.64%	0.62%	0.20%	9.2 kN 9.7 kN 9.4 kN

Chemical compound and breaking force of investigated KSAN 3,5 cable specimens

Endurance tests

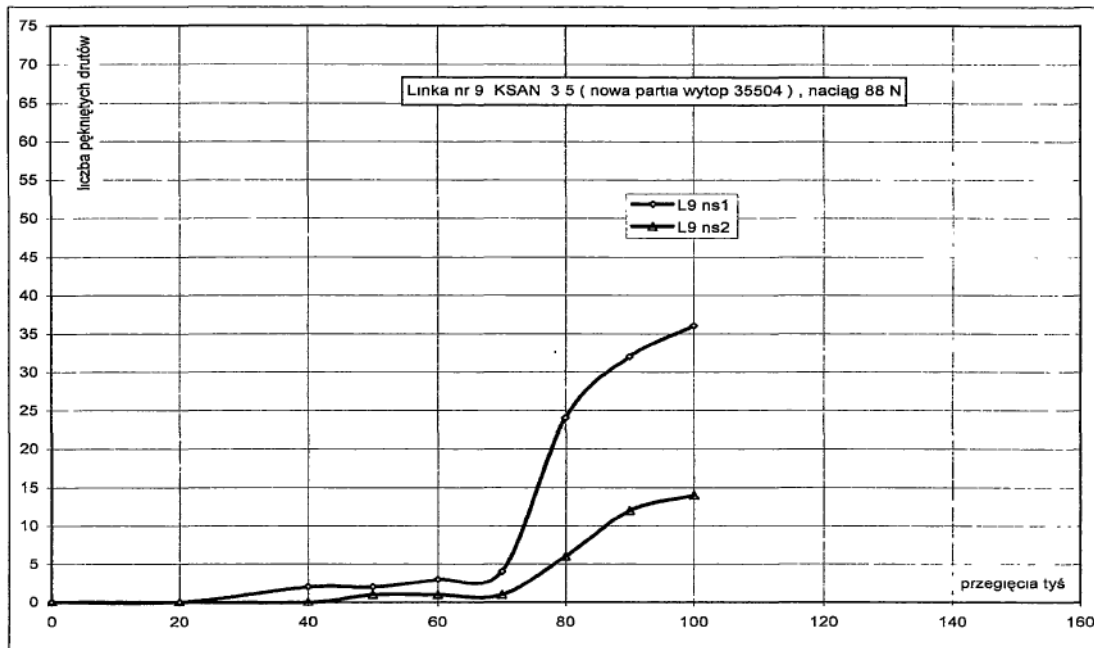
Extensive endurance tests of the KSAN 3,5 cable specimens were performed in the PZL MIELEC test laboratory. Simple stress analysis of the aircraft control system cables showed that cyclic bending of the rope on the pulleys was the main contributor to wires fatigue damage. The tests were performed both under the conditions as in the standard, and under the conditions more closely reflecting those in the PZL M28 aircraft. The test rig allowed the implementation of test sheaves of different diameters and different tension loads.



Scheme of the test rig for cable specimens endurance tests. “Upper” and “lower “ sheaves are visible as attached to the wall at left (see “rolka I” and “rolka II” on figure, respectively). The cable was put in motion through the eccentricity. Rubber hose (see “sprężyna gumowa” on figure) was used to maintain constant tension. Usually, the cable specimen length allowed test to be performed on both sheaves

Endurance tests performed under the conditions as in the standard

Endurance tests under the conditions as in the standard TU14-4-1266-83 (test sheave diameter 35 mm, tension load 88 N) were performed on one cable. The cable was bent by 90 degrees on two sheaves of the same diameter, referred to as “upper” and “lower” following the test rig arrangement, so two results of the test were obtained. Number of reverses according to the standard is 70 000, but test was conducted up to 100 000 reverses. Number of broken wires was observed after 20 000, 40 000, 50 000, 60 000, 70 000, 80 000, 90 000 and 100 000 reverses. “L9 ns1” refers to the “upper” sheave, while “L9 ns2” refers to the “lower” sheave.



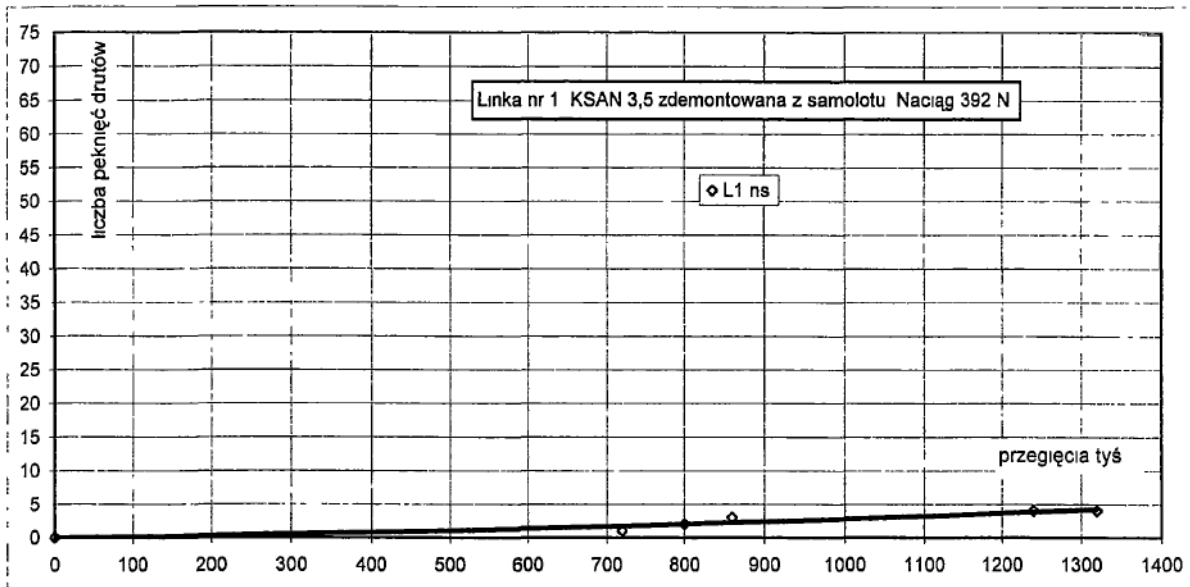
Test result of the KSAN 3,5 cable specimen number L9 (“Linka nr 9 KSAN 3,5...”) endurance test performed according to the standard TU14-4-1266-83. Number of thousands of reverses is on horizontal axis, while number of broken wires is on vertical axis. Test was conducted up to 100 000 reverses. Results refer to “upper” and “lower” sheave

As presented in figure, the test result was positive, as at 70 000 performed reverses number of broken wires at the “upper” sheave was 4, while on the “lower” sheave was 1. Breaking force after 70 000 reverses was not measured as it would prevent further test conduction. A small number of broken wires after 70 000 reverses indicated the fulfillment of the breaking forces condition.

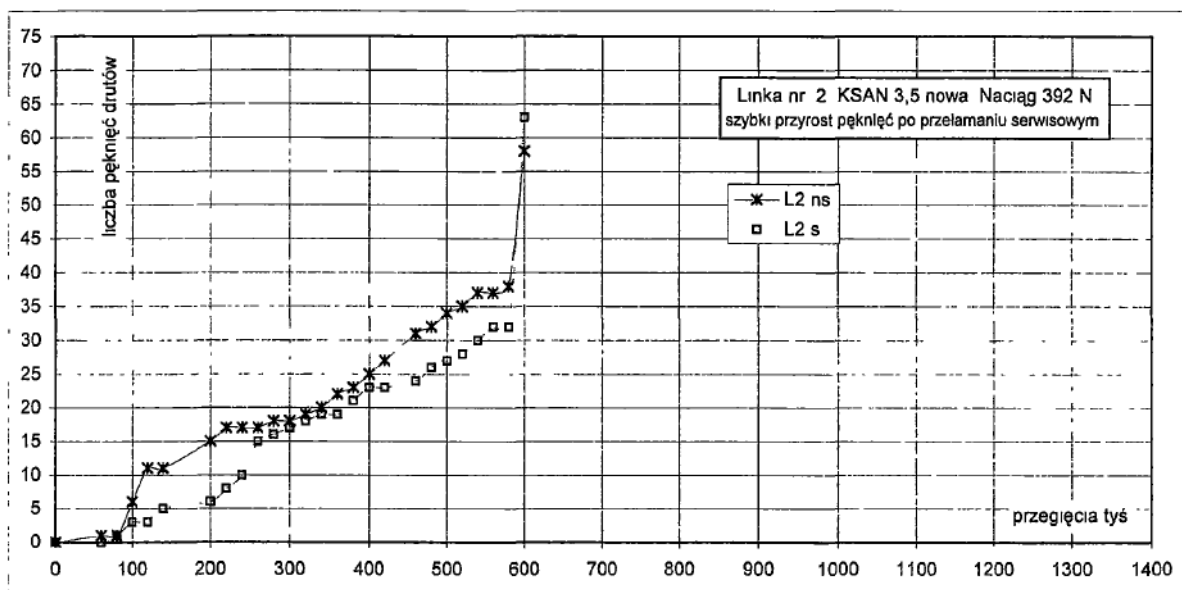
This test also showed a significant increase in the number of broken wires after 70 000 reverses, and significant scatter of the result between the “upper” and “lower” sheaves.

Endurance tests performed under the PZL M28 conditions

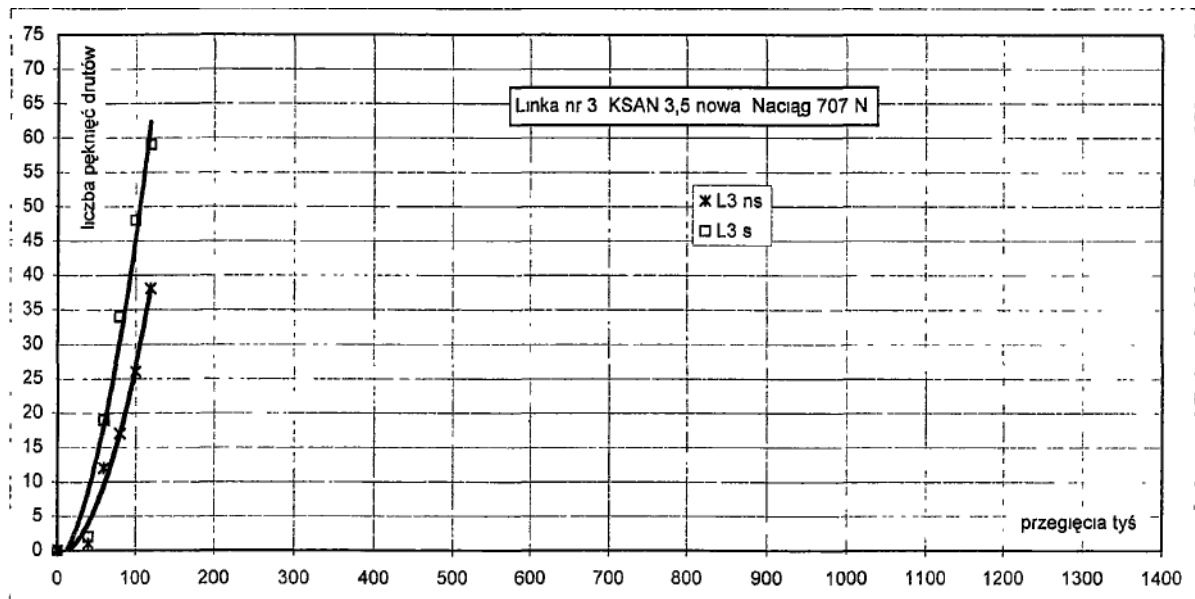
Endurance tests under the conditions reflecting those on the PZL M28 aircraft were performed with test sheaves diameter 64 mm. Tension load was 392 N (nominal tension in the cable control system of PZL M28 in RT) or 707 N (tension measured in the cable control systems of some PZL M28 family airplanes). In total, 8 cable specimens were tested. In some cases, the cable was lubricated with grease for research purposes only (it is not allowed to be done by cable manufacturers). In each case the test was conducted until a significant number of broken wires, but in one case up to 1 320 000 reverses number of broken wires rose to 4 only.



Test result of the KSAN 3,5 cable specimen number L1 (“Linka nr 1 KSAN 3,5 ...”) endurance test performed for sheaves diameter 64 mm and tension load 392 N. Number of thousands of reverses is on horizontal axis, while number of broken wires is on vertical axis. Small length of this specimen caused that cable was bent only on one sheave. Test was conducted up to 1 320 000 reverses. Number of broken wires at the end of test was 4



Test result of the KSAN 3,5 cable specimen number L2 (“Linka nr 2 KSAN 3,5 ...”) endurance test performed for sheaves diameter 64 mm and tension load 392 N. Number of thousands of reverses is on horizontal axis, while number of broken wires is on vertical axis. Cable was bent on two sheaves. Test was conducted up to 600 000 reverses. Part of the cable (“lower” sheave) was lubricated by grease; number of broken wires for this part is labeled as “L2 s” on the figure, while number for not lubricated part is labeled as “L2 ns”



Test result of the KSAN 3,5 cable specimen number L3 (“Linka nr 3 KSAN 3,5 ...”) endurance test performed for sheaves diameter 64 mm and tension load 707 N. Number of thousands of reversals is on horizontal axis, while number of broken wires is on vertical axis. Cable was bent on two sheaves. Test was conducted up to 140 000 reversals. Part of the cable (“lower” sheave) was lubricated with grease; the number of broken wires for this part is designated as “L3 s”, while the number for the unlubricated part is designated as “L3 ns”

Scatter of test results is shown in tables below.

Tension load 392 N		
Number of test result	Number of reversals for 1 wire broken observed	Number of reversals for 27 wires broken observed
L1ns	720 000	
L2ns	60 000	420 000
L5ns1	40 000	500 000
L5ns2	40 000	300 000
L6ns	80 000	1 300 000
L10ns1	40 000	300 000
L10ns2	40 000	
mean	145 714	564 000
standard deviation	234 877	375 745

Test result of the KSAN 3,5 cable specimens endurance test performed for sheaves diameter 64 mm and tension load 392 N as number of reversals for 1 wire broken observed and 27 wires broken observed. For specimens “L1ns” and “L10ns2” number of broken wires during test was lower than 27

Tension load 707 N		
Number of test result	Number of reversals for 1 wire broken observed	Number of reversals for 27 wires broken observed
L3ns	40 000	100 000
L4ns1	40 000	80 000
L4ns2	40 000	120 000
L11ns1	60 000	
L11ns2	20 000	140 000
mean	40 000	110 000
standard deviation	12 649	22 361

Test result of the KSAN 3,5 cable specimens endurance test performed for sheaves diameter 64 mm and tension load 707 N as number of reversals for 1 wire broken observed and 27 wires broken observed. For specimen "L11ns1" number of broken wires during test was lower than 27

Test results showed significant scatter, which was larger for tension load 392 N. Standard deviation of the test results rose with the number of broken wires, but on the other hand the coefficient of variance (ratio of standard deviation and mean value) decreased with the number of broken wires. Of course, limited confidence should be paid for the moment when the first broken wire is observed.

Another observation is that intensity of fatigue damage of wires is significantly influenced by tension load. Although stress analysis does not support this observation, as it indicates a low contribution of tension load to stress level in wires.

Notes about inspection of tension in aircraft control cables and aircraft maintenance recommendations

A significant impact of tension load in the control system cable on the result of the endurance test made the researchers check the real tension load in PZL M28 family cable control systems. Checking the tension with the instruments used by the PZL service resulted in obtaining significantly higher tension values than those given in the aircraft maintenance instruction.

During maintenance inspection, a cable tension meter is in common use. Tension meter manufacturers give important notices about the calibration of the instrument and cable tension measurement in aircraft systems. Improper calibration can give false reading of the tension. According to tension meter producer, the simple method that gives a reliable result is a dead weight arrangement. This may be also done in a testing machine against a hydraulic gauge.

Another issue is that cable tension readings taken on regulated control systems by means of a tension meter could be misleading as the use of the instrument influences tension. Tension measurement has to be adjusted to the particular control system.



Pacific Scientific Co. T5 cable tension meter

After the PZL M28 military operator implemented a new method of tension meter calibration, the number of broken wires in the fleet observed during periodic maintenance inspection decreased to the usual level.

Conclusions

Steel wire ropes were developed in the 19th century. First stress analyses were performed also at that time. Although issues related to the use of wire ropes in various systems - including cableways, elevators and mining - have been well recognized in more than a century, accidents still occur - including air accidents caused by control system cable damage. This means that one must always follow strict rules for the use of wire ropes, e.g. in aircraft control systems, and analyze their operating conditions on an ongoing basis during the operation of the aircraft.

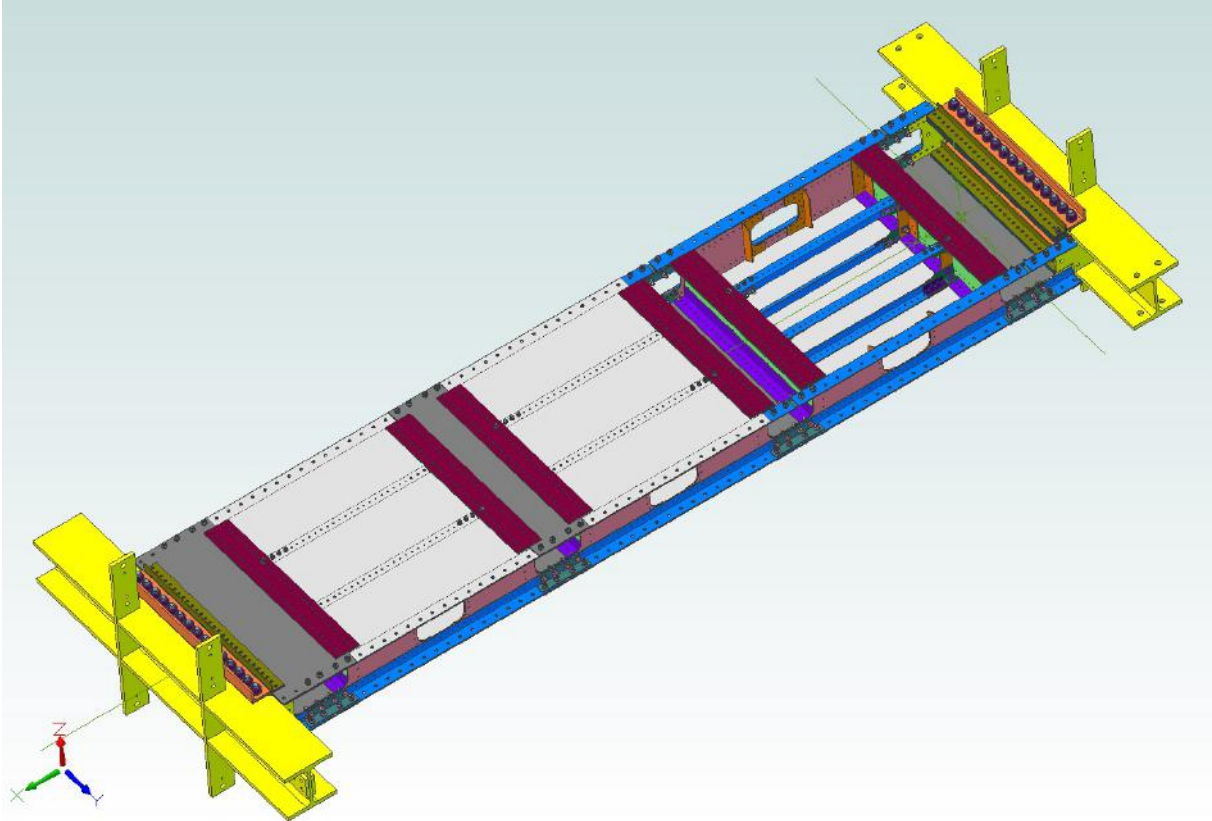
The influence of the cable tension on the result of durability tests, which is not confirmed in the wires stress analysis, is surprising. It is likely to be caused by the stochastic nature of damage to the wires of the cable during cyclic bending.

Conception of Modular Test Stand for Fatigue Testing of Aeronautical Structures

Fatigue tests of specimens and components are necessary part of an aircraft development as well as an introduction of new improvements and solutions into aircraft structures. Despite the enormous development of methods of analysis, experimental testing remains the primary method of proving fatigue strength. This is caused by the risk of a crash in the case of failure, as well as a limited ability to properly identify fatigue behavior through analysis. At the same time fatigue tests are definitely more expensive than static since they are more complicated and last longer. The majority of fatigue tests are conducted on testing machines with simple specimens, usually with loads restricted to tension. Introduction of a more complex state of loads (compression, torsion and bending) requires preparation of more complicated specimens (e.g. sub-components) and dedicated testing stands.

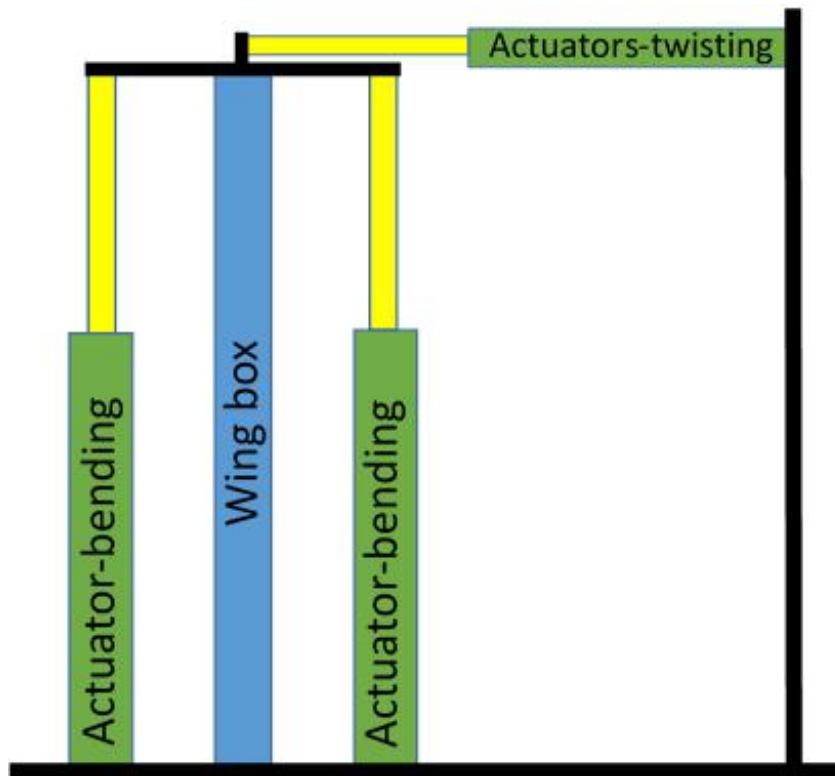
The Modular Test Stand (MTD) was proposed by the authors to decrease cost of fatigue tests and enable simple specimens to be tested in more complex load states. The conception assumes that during a one experiment several specimens can be tested and it is possible to test a simple specimen that is mounted into a more complex structure. The MTD consists of three

identical sections, which are connected in such a way that each section is loaded in the same manner, as well as of fixing and loading system. The section is a structure similar to airframe, namely wing box, and consists of two spars, ribs and flat skins. The whole section, a structural node, particular joint or a skin can be an object of testing. The one section has a dimension of 600 x 600 x 150 mm. Each of the section can be quite easily disconnected and exchanged. It is also possible to use one or two sections only. Figure below presents the model of three sections (wing box) connected with fixings.



Three sections with fixing

The stand enables to load sections with a bending or twisting moment (not simultaneously). One end is fixed and the second is loaded with a moment induced by two hydraulic actuators. The moment is constant along the wingspan. The wing box and the actuators generating bending are vertical. This configuration facilitates access to the specimen (e.g. during inspections) and eliminates necessity of balancing vertical actuators.



Configuration of Stand

The proposed stand can be used to determine fatigue behavior of whole sections (e.g. made in various technology), design of selected structural nodes, joining methods (e.g. riveting, bonding, Friction Stir Welding, etc.) or materials (metal, composite, FML). The MTD can be used also for fatigue tests of structures with damages or repairs (e.g. composite patch repairs) as well as with various types of sensors (e.g. used for Structural Health Monitoring). The advantages are a lower cost and a more complex load state compared to simple specimens.

The modular Test Stand has been design with the use of FE analyses in order to obtained quite uniform stress distribution in the tensioned skin under bending, with the assumed level of 120 MPa. Additional limitations were the force and displacement ranges of the selected actuators (25 kN/500 mm). After manufacturing and installation, the stand was statically loaded with a bending moment. The obtained displacements and strain distribution were verified with the use of full-field measurement method (Digital Image Correlation) and strain gauges.

INVESTIGATIONS IN MILITARY AVIATION

STRUCTURAL LOAD / USAGE / HEALTH MONITORING

Operational Load Monitoring System for Su-22UM3K fighter - bomber

The in-service usage monitoring is an important airworthiness requirement to handle safety of the aircraft, as the load and fatigue spectra change during long-term operational use due to numerous factors. The approach for this purpose has evolved from g-counters to modern on board parametric systems incorporating several aspects e.g. material fatigue, measurement techniques, signal analysis, modelling etc. All that to increase the safety and extending the life of the aircraft. Regarding the above, Individual Aircraft Tracking (IAT) with use of Operational Load Monitoring (OLM) system is essential to ensure the implementation of the maintenance and utilization strategy. Moreover, the OLM also allow the use of usually significant functional potential for the ageing aircraft, which, after performing the necessary renovation, will allow their further operation according to the technical condition.

In 2014 Polish Air Force decided to continue the operation of the ageing Su-22 “Fitter” fighter-bomber based on Service Life Extension Program. The aircraft has been in service in Poland since the 1970s. In total, 110 Su-22 aircraft were in use in the Polish Air Force in two variants: Su-22M4 combat version and the Su-22UM3K twin-seat trainer. Air Force Institute of Technology in cooperation with Military Aviation Works no. 2 JSC performed the implementation of an structural integrity and modernization program aimed for continuation of Su-22 operational use for another 10 years.

At present, Individual Aircraft Tracking (IAT) with use of Operational Load Monitoring (OLM) system is essential to ensure the implementation of the maintenance and utilization strategy. Moreover, the OLM also allow to use of usually significant functional potential for the ageing aircraft, which, after performing the necessary renovation, will allow their further operation according to the technical condition. Such a system combines flight parameters from Flight Data Recorders with acceleration and strain/stress data from the structure “hot spots” measured in real time to determine loads and usage factors of an individual aircraft.

The implementation of the OLM system for Su-22UM3K twin-seated combat-trainer aircraft will be presented. Its purpose is to assist their operational use and enable controlled and safe utilization within a period of prolonged service life above 3200 flight hours and 6000 landing number. The system collects strain and acceleration data from pre-defined localization on the airframe in real time - wing main spars, main landing gear main strut and main landing gear-wing connection point. Sensors are installed symmetrically on both sides of the aircraft to be sensitive for asymmetrical loading as well as redundancy. Data are post-processed and analyzed periodically on the ground station, to reveal operational loads and detect exceedances both in the air and during landings.

Based on in-flight data from the OLM system, load determinations from typical maneuvers are presented. The individual tracking of usage parameters, like fatigue usage, operational intensity and equivalent-to-real flight hours can be performed for separate aircraft as well as detecting the operational exceedances and quantifying their influence on aircraft durability.

Regarding ageing aircraft, they are now expected to last much longer than first envisaged. Strain based in-flight data recorders are perceived to provide more accuracy over the conventional fatigue g-meter, and have thus been implemented worldwide by many military fleet operators.

Concept of Health Monitoring System for Mi-8 Helicopter with Integrated Sensors

Structural integrity and usage monitoring is one of the key issues in the process of the helicopter service life. Such a system should detect operational exceedances as harsh landing which occur randomly as well as failure of critical elements due to fatigue and vibration. In the paper, the concept of health and usage monitoring system for Mi-8 helicopter is presented. Additionally, some results from experiments performed previously (e.g. full scale drop test) will be described to confirm design concept.

The proposed system is based on additional on-board data recorder with integrated sensor network of different type. In a presented concept, 12 IEPE accelerometers are installed on main gearbox, rotor brake, hanger bearings, intermediate and tail rotor gearbox. Additionally, 3-axis MEMS accelerometers are mounted in the bottom of the cockpit, top of the tail rotor. One installed near center of mass is equipped with additional 3-axis gyro. Also 12 strain gauge channels are used in critical structural elements, like front landing gear, two main frames and fuselage-tail boom connection to monitor loads during flight. Two distance sensors mounted in front and rear fuselage will give the information of landing speed.

Data recorder has an open architecture with exchangeable measuring user modules, as the number and type of measuring channels can be easily reconfigured to add more sensors if needed. The recorder also has a built-in GPS to acquire navigation parameters for complete data analysis. The prototype installation is being performed on the Mi-8 helicopter during its overhaul, and the system is about to become operational. IEPE and MEMS accelerometers locations were selected based on helicopter design, experience and literature. Strain gauges locations were already tested and confirmed during other experiments, which results will be briefly presented in the paper.

The purpose of the proposed monitoring system is to increase safety of operational use of the Mi-8 helicopter by detecting exceedance during flight as well as failures in drive train and rotor system.

SHM application to Remotely Piloted Aircraft Systems - SAMAS
European Defence Agency Ad Hoc Category B Project n° B-1404-ESM2-GP



Project consortium:

Politecnico di Milano (IT) – consortium leader
Leonardo S.p.A (IT)
Instytut Techniczny Wojsk Lotniczych (PL)
Wojskowe Zakłady Lotnicze nr 1 S.A. oddział w Dęblinie (PL)

Project duration:

Dec 2017 – Dec 2020

The use of Remotely Piloted Aircraft Systems (RPAS) is nowadays growing and a recent market study estimates that the spending on RPAS will almost double over the next decade [1]. They offer the possibility to extend the duration of vehicles as well as the acceptance of high risk mission profiles, due to the absence of a pilot. Furthermore, the absence of any limit on performances imposed by the survivability of the pilot is an additional aspect, especially desired for military applications. RPAS have been used in segregated airspace for many years. Nevertheless a big advantage will result from the possibility to extend their usage beyond line of sight in the non-segregated airspace within any specified area of operations. Their utilization would be not only connected to military purposes but also to security related, scientific and environmental missions. Nevertheless, the absence of any physical pilot poses some new challenges that have to be addressed through applied research. In particular, bird strike, lightning strike, battle damage and damage during taxi or landing are just few of the conditions that in general are assessed by the pilot in a manned aircraft while they have to be identified through a smart sensing and reasoning system on board in a RPAS [2]. Furthermore, fatigue damage is an additional obstacle that increases the maintenance requirements for such flying structures. In June 2014, the Washington Post reported [3] that more than 400 large U.S. military drones have crashed in major accidents around the world since 2001, thus exposing the potential danger related to drone traffic, according to a year-long Washington Post investigation. In particular military drones have failed due to a large number of reasons, mainly connected with the following points: (I) a limited ability to detect and avoid troubles, (II) pilot errors, (III) persistent mechanical defects and (IV) unreliable communication links.

SAMAS is the third project coordinated by Politecnico di Milano (Department of Mechanical Engineering) within the European Defence Agency (EDA) and focusing on structural health monitoring. The first project, HECTOR (Helicopter crack monitoring system and prognosis through on-board sensor network [4]) was concluded in December 2011 and

served as a starting point for methodology setup. SHM was applied to metallic structures and a demonstrator of the diagnostic system for fatigue crack detection, localization, quantification and prognosis has been provided as main activity output. The natural prosecution of the HECTOR project is ASTYANAX (Aircraft fuselage crack monitoring sYstem And progNosis through onboArd eXpert sensor network [5]). This project ended in December 2015 and its goal was the exploitation of the HECTOR methodology for both harsh landing monitoring and fatigue crack monitoring. Though the SHM is still applied to metallic structures, the systems have been deployed on full-scale laboratory tests, thus increasing the TRL of the activities. The overall experience gained in the two previous projects will be exploited in the present project. SAMAS activities will be focused on composite structure monitoring, specifically concerning the application to unmanned aircraft systems. The project scope is very broad and includes three main objectives:

- the realization of an efficient load monitoring system composed by real and virtual sensor nodes. This system will be tested on ground in a laboratory environment on a full-scale RPA structural component as well as during flight tests on a small scale RPA.
- the development of an impact monitoring system able to detect the occurrence of the impact, to characterize the impact (in terms of location and energy) and to estimate and verify the occurrence of impact damage. This system will be tested in a laboratory environment on a full-scale RPA structural component.
- the verification of SAMAS activities with respect to certification aspects will be the third milestone of the project, with reference to the currently available guidelines and recommendations for the HUMS implementation and integration (e.g. ARP6461, EMACC).

Additionally, in conjunction with the Customers, a particular attention will be placed on the economic advantages derived from the SHM tool application on RPAS in service, with a Cost and Benefit Analysis and an evaluation of the Life Cycle Cost in comparison with the traditional one (operating and support, including current maintenance and overhaul schedule, service life, flights preparation, etc.).

The expected TRL of the systems developed in the framework of the SAMAS activities is 6 to 7 for load monitoring and 4 to 5 for impact monitoring. The main goal of the project is the assessment of the feasibility of a multi-purpose sensor network which can be exploited for both load monitoring and impact monitoring. It was demonstrated before that FBG technology can be fitted to perform load monitoring, thus enabling the estimation of fatigue life consumption, impact monitoring (through high-frequency acquisition) and fatigue damage detection and assessment as well. The latter was preliminarily accomplished in previous projects by the same contractor (HECTOR [4] and ASTYANAX [5]). Additional promising technologies which are also investigated are mainly focused on piezo-electric sensors for impact detection and impact damage verification based on guided waves actuation and sensing.

The SAMAS project will demonstrate the objectives mentioned above across two levels:

- 1) By conducting “System Demonstration” which will allow the testing and validation of the proposed system. Real-life use case scenarios are foreseen for each of the project objectives and will be defined with the Customers of the consortium.
- 2) By “System Simulation”, aimed at supporting the development and check the robustness of the innovation under controlled conditions to reduce the risk associated to the conduct on flight testing and to enable the extrapolation of the real life testing to a wider set of conditions than those covered by the in-flight system demonstrations.

USE CASE 1 – Load monitoring system. The first stream of the project is dedicated to RPA on-board load monitoring. Two types of sensor technologies have been identified for load

monitoring application. First, a network of multiplexed FBGs will be deployed on a selected composite structural part of a RPAS platform. Second, tri-axial accelerometers will be installed in some areas within the RPA structure. Numerical models (mainly Finite Element Models) will be used for a dual purpose:

- 1) To optimize sensor positions on the structure, thus selecting those zones that contain most information about contingent loads.
- 2) To create a database of strain patterns as a function of different aircrafts manoeuvres.

As a matter of fact, it is reasonable to assume that manoeuvre loads are the most responsible for structural damage evolution. Nevertheless, points of interest within the aircraft for structure degradation are widespread and it is often impractical to cover each zone with a sensor to measure the exact usage of the particular structure or component at sensor location. Thus, assuming the maneuver can be correctly identified based on a restricted number of sensors, numerical models can be used to extrapolate the value of strain from sensor location to the node of interest. It is clear that this methodology is based on a limited number of sensors but poses no limits in the number of virtual sensors within the structure. Linear and non-linear methods for the evaluation of life consumption can thus be adopted for each location of interest, and composite structures will be taken into consideration. Both ground and flight test campaign are considered. Ground tests will be performed on a composite component of a RPA structure and comprehend:

- data storage on a desktop-PC;
- feature extraction with dedicated signal processing algorithms for load monitoring;
- diagnosis of damage evolution under spectrum load (as a matter of fact the same component will be tested under impact loads, as described below).

Flight tests will be performed to test the load monitoring system on-board of a reduced size RPAS (HORNET platform) with 3.2 m wingspan, 2000 m service ceiling and 30 km service range. Before the flight tests, a ground test campaign on the same RPAS platform (HORNET) will be arranged to evaluate the response of the sensor network under different types of applied load (representative of the main maneuvers).

USE CASE 2 – Impact and damage monitoring system. The second purpose of the project is aimed at integrating NDE sensing with RPA structure, enabling to detect the occurrence of an impact, as well as to sense the generation of such structural defects as delamination and disbonds. Basically, the complete solution of the impact monitoring problem consists of three steps:

- 1) Impact detection and assessment. Passive sensors are used to sense the acoustic waves travelling in the material as a consequence of impact and provide indication of impact occurrence, impact location and impact energy.
- 2) Virtual impact damage assessment. A database of numerical impact simulations on specimen coupons similar to the operative structure is used to provide indication of damage occurrence because of the impact. Basically, assuming impact energy is known from a passive monitoring system, an estimation of impact damage extent will be provided.
- 3) Impact damage verification. Active piezoelectric sensors will be used to effectively check whether the structure is damaged or not, thus providing a verification of the assumption made at step previous step – no 2.

It has been demonstrated in previous research activities that high frequency acquisition (up to 100 kHz) from FBG sensor network (as well as from a PZT sensor network) would allow to identify the occurrence of impacts on the monitored structure (passive sensing technique). The idea in SAMAS is to estimate the impact damage based on simple virtual coupon specimens representative of the area being inspected and knowing the output from the passive

monitoring system (in terms of location and energy of the impact). Verification of the impact damage based on guided waves is proposed [6] as an active system. Piezoelectric sensors can be used to detect variations in structural and material properties for structural health monitoring. Impact damage can sometimes induce barely visible impact damage (BVID) in the structure, which affects the selected acoustic wave mode propagation, thus changing the wave velocity or producing wave mode conversion. Analysis of such phenomena is based on specially designed algorithms such as wavelets, short time Fourier transform (STFT) and specially designed inference models allows for automated damage detection of the impact damage.

References

- [1] Zaloga SJ, Rockwell D, Finnegan P. World Unmanned Aerial Vehicle Systems, Market Profile and Forecast (2011 edn). Teal Group Co.: Fairfax, Virginia, USA, 2011.
- [2] Buderath M, Neumair M. Operational Risk Assessment for unmanned aircraft vehicles by using structural health and event management. EADS Military Air Systems D-81663 München, 2007.
- [3] Washington Post, 20 June 2014, When drones fall from the sky, Craig Whitlock.
- [4] HECTOR - Helicopter crack monitoring system and prognosis through on-board sensor network, Contract JIPICET A 0930 RT GC.
- [5] ASTYANAX – Aircraft fuselage crack monitoring system and prognosis through on-board expert sensor network, Contract No B 1288 ESM2 GP.
- [6] Dziendzikowski, M., Kurnyta, A., Dragan, K., Kłysz, S., Leski A. In situ Barely Visible Impact Damage detection and localization for composite structures using surface mounted and embedded PZT transducers: A comparative study. *Mechanical Systems and Signal Processing* 78 (2016): 91-106.

FULL SCALE TESTING

Evaluation of the suitability of a strain-gauge method for measuring deformations within the fatigue tests of aviation composite structures

Introduction

Composite materials, which are currently more and more commonly used in aviation structures, also in primary elements, should be effectively diagnosed in the course of their operation. Their diagnostic process is hindered due to the process of fatigue damage formation and development, which is different than in metallic materials. Their hard to detect nature, frequent lack of surface signs of fatigue, the presence of damage in the form of intra-bedding or inter-bedding delamination, and a very rapid damage process of cyclically loaded material, enforce an intensive development of diagnostic methods, effective not only in the process of composite aviation structures maintenance, but also within their operating process [1, 2, 4].

The group of relatively cheap methods for analyzing composite structures includes a procedure based on measuring deformations with the use of strain gauges. The method can be used both at low, as well as high temperatures, under changing pressure or at high humidity. An additional advantage of this method is also the fact that the fastened sensors do not affect the continuity of a structure, and do not adversely impact the strength parameters of a material [6, 7, 8]. The number of sensors to be installed on a diagnosed element depends on many factors. Modern calculating tools based on the finite elements method can be used for the difficult task of selecting the number of strain gauges and their installation locations [5]. They can be used to select the locations, in which deformation change measurement will “generate” the most effective diagnostic information.

The objective of the conducted tests was the assessment of the possibility to use the strain gauge method as a diagnostic tool in evaluating the technical condition of a primary composite aviation structure - an aviation spar. Because the weak spot in composite structure are the nodes “transferring” concentrated loads, the diagnostic process in the presented analysis, mainly concerned two spar nodes, with used non-adhesive metal-composite joint. The conducted diagnostic tests based on strain sensors were supplemented with thermography tests with the use of a thermal imaging camera.

Experimental tests

Own tests involved using a composite spar of an AOS-71 glider. The spar was constructed in composite technology, so-called wet carbon fibres and carbon roving [3]. We can distinguish three structural elements of the spar: a pin with fittings, spar caps and a wall with reinforcement. The cross-section of the spar has the form of a double-tee bar. Figure 1 shows the spar model with its main dimensions.

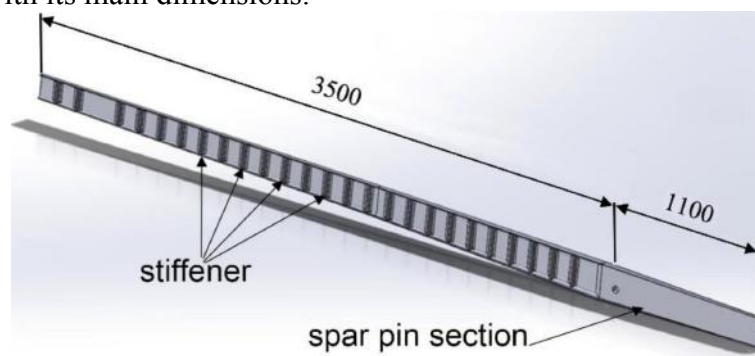


Figure 1. Spar model

A test bench was designed and constructed for the purpose of the experimental tests. The tested composite spar was mounted on a load floor with two triangular supports. The spar movement in all three planes was restricted in the support of node no. 2, while the movement of the spar in the spar wall plane was enabled in the support of node no. 1. This method of spar mounting corresponds to the spar installation conditions in a motor glider.

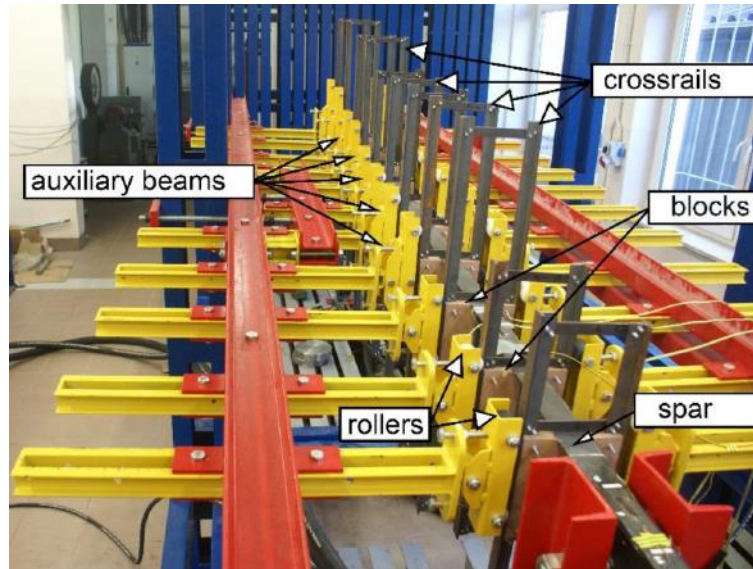


Figure 2. The method for mounting the spar on the test bench

The composite spar was cyclically loaded with a Bosch Rexroth hydraulic cylinder, fastened from one side to a load floor and to the spar from the other side, using a special clamp. A force gauge was also attached to the cylinder, for use in the load control system

Spar deformations at selected locations, the force and spar displacement over the cylinder plane were recorded during the fatigue tests. A tensometric system used for measuring the deformations utilized 19 sensors, including: 15 strain gauges with a 300 Ohm specific resistance and 4 strain gauges with a 120 Ohm specific resistance

Results of experimental tests

The execution of the experimental tests provided deformation change courses, the nature of which corresponded to a spar swing load cycle. Six deformation values in individual measuring channels were recorded for half of the cycle. Examples for deformation change course for the 1st, 500th and 1000th cycle in 16 measuring channels are shown in Figure 3.

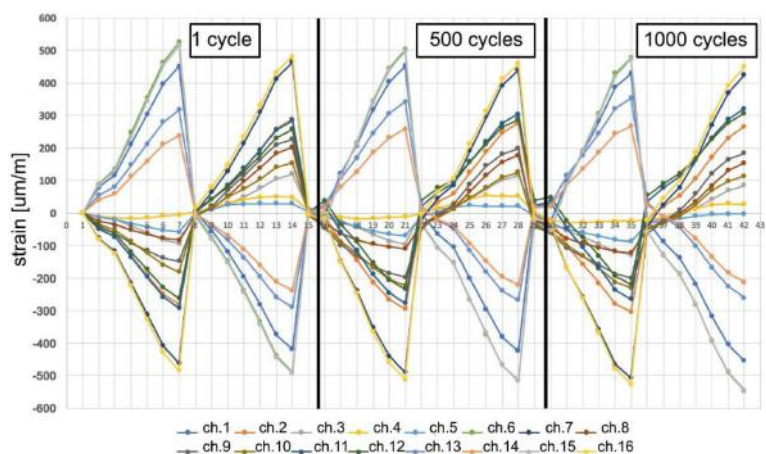


Figure 3. Course of deformation changes

Literature

- [1] Glass Andrzej, Murawski Tomasz: „Polskie szybowce 1945-2011. Problemy rozwoju” [Polish gliders 1945-2011. Development issues], Wydawnictwo SCG.
- [2] Rodzewicz Mirosław: „Spektra obciążeń i trwałość zmęczeniowa struktury nośnej szybowców kompozytowych” [Load spectra and fatigue durability of a composite glider load-bearing structure], Oficyna Wydawnicza Politechniki Warszawskiej.
- [3] „Technologia ramowa wykonania dźwigarów skrzydeł” [Frame technology for the execution of wing spars], Politechnika Warszawska, Warszawa, listopad 2010.
- [4] Orkisz Marek, Święch Łukasz, Zacharzewski Jan: „Badania zmęczeniowe kompozytowego dźwigara skrzydła motoszybowca” [Fatigue tests of a motor glider wing composite spar].
- [5] Łaczek Stanisław: „Przykłady analizy konstrukcji w systemie MES Ansys-Workbench V.12.1” [Examples of structural analysis in the MES Ansys-Workbench V.12.1 system], Wydawnictwo Politechniki Krakowskiej.
- [6] Roliński Zygmunt: „Tensometria oporowa. Podstawy teoretyczne i przykłady zastosowań” [Resistance tensometry. Theoretical basis and examples of application], Wydawnictwa Naukowo-Techniczne, Warszawa 1981.
- [7] Praca zbiorowa: „Mechanika techniczna. Laboratorium” [Technical mechanics. Laboratory], Oficyna Wydawnicza Politechniki Warszawskiej, Warszawa 2000.
- [8] Sen Lin: „Strain Measurement by Digital Image Correlation”, Royal Institute of Technology, Sweden 2015.

ADHESIVELY BONDED STRUCTURES

The repair design and technology of metal rotor blades for Mi family helicopter – the approach with the usage of reverse engineering

Introduction

Mi family helicopters were designed in Soviet Union, Poland and were produced there. All of the Warsaw Pact Organization countries used many types of these helicopters. After dividing of Soviet Union, those vehicles, despite archaic appearance, are still being produced due to the fact that they possess exceptionally good operational characteristics in military and civil usage. Semi monocoque construction is simple and relatively easy to repair. Durable engines are capable of work in cold Syberian temperatures, as well as in aggressive desert conditions – high temperature and dust. In the Polish Air Forces still uses Mi-2, Mi-8, Mi-17, Mi-14 and Mi-24.

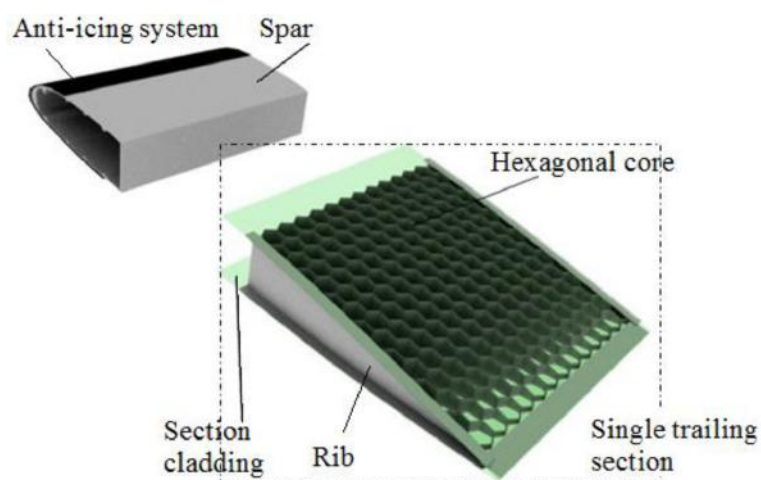


Figure 4. Schematic construction of a single section of rotor blade

The purpose of work

Main aim of carried work was to develop a construction project and technology of described damages with an use of adhesive joining and polymer composites. Important point of work was presenting the repair substantiation as well. The assumption was that developed technology could allow repair without necessity of section exchanging, as well as applied technology will not cause danger of material changes in spar.

Fundamental research

The research was mainly focused on the selection of proper adhesive. The main parameter on which the selection was based, was the maximal cure cycle temperature (below 130°C). Reducing the temperature of the curing cycle from 190°C, which is required to cure the original adhesive, down to 120°C allows multiple repairs, without risking of thermal damage of the spar. The research had a comparative nature. Three adhesives were tested: original thermoset film, replacement film adhesive, and chemically hardened adhesive paste. Bonding surface of aluminum was prepared with PAA anodizing and with an use of Sol-Gel technology (SG).

Fatigue test

The last part of ground testing, according to the diagram (Figure 4), is fatigue test. Research is carried out on a dedicated for this purpose test rig of four-point bending with load spectrum presented earlier. Loads are carried out with a frequency of 1.3 Hz. Each patch is provided with a strain gauge. This test will require at least two samples, undamaged and repaired, to acquire sufficient amount of data.



Figure 5. Test rig for fatigue test of rotor blade sample.

Summary

The article presents authors approach in a development of repair technology in AFIT. Developed approach by the authors has a target to systematize the process of designing repair for various types of aircraft, even in the case when there is no access to complete documentation of the structure. Versatility of the process has been verified during this project.

NON-DESTRUCTIVE EVALUATION

Analysis of Adhesive Disbond Occurrences in Rotor Blades of Mi-2 Helicopters

Polish Air Force Institute of Technology (AFIT) is responsible for delivery service life extension program for the main rotor blades of multiple helicopters in the Polish Air Force (such as Mi-2, Mi-8/17, Mi-14, Mi-24). Due to the operational profile, certain number of blades got decommissioned when the calendar service life is reached, while the accumulated flight hour count is still below the hourly service limit. This is why a dedicated research program, as well as inquiry into the usage and technical condition of the blades is necessary. To maintain such a program, regular inspections of the blade structure are required.



Figure 6. MIA testing using MAUS

Since 2007 in the Air Force Institute of Technology ongoing work related to the helicopters main rotor blades service life extension. These include all types of the Mi helicopters main rotor blades [3, 5]. Main reason for starting that program was that a lot of rotor blades have to be removed from operation despite of time of life still remained (in average 40%). As result of research project a program of service life extension based on so called calendar has been developed.

This program was implemented in three phases for a total of 42 months of service life extension. Since 2007, the program helped to extend the resources of dozens of blades any types of the Mi helicopters. It is based on non-destructive tests, in accordance with elaborated in AFIT procedures.

The most common type of failure mode on Mi-2 rotor blades is disbonded between skin and spar. According to AFIT procedures, section skin to spar disbond detection is made with Mechanical Impedance Analysis method using Boeing MAUS V system shown on figure above. During analysis of non-destructive results, authors observed a clear difference between the number of disbonds on the lower and upper surface of the blade. Moreover it has been observed that the greatest concentration of damage is near the axis of the rotor on lower surface. Most likely, this is due to presence of water inside rotor blades. Mi helicopters family rotor blades design assumed the possibility of migration and storage of water.

References

- [1] Adams D., O., DeVries K. L., Child C., “DURABILITY OF ADHESIVELY BONDED JOINTS FOR AIRCRAFT STRUCTURES”, JAMS 2012 Baltimore.
- [2] Bartholomeusz R.A., “Reduction of shear and flatwise tension strength in F-111 honeycomb panels exposed to moisture”, DSTO-TR1331, Australia, 2002.
- [3] Dragan K. “NDE activities connected with Service Life Extension of Main Rotor Blades of Helicopters used in Polish Armed Forces.” 7th Australian Pacific Vertiflite Conference on Helicopter Technology, 2009, Melbourne.
- [4] Ebnesajjad S., “Adhesives Technology Handbook”, Norwich, NY, USA: Wiliam Andrew Inc., 2008, pp. 231–232.
- [5] Niepokólczycki A., Leski A., Dragan K., “Review of aeronautical fatigue investigations in poland (2013-2014)”, Fatigue of Aircraft Structures Vol. 1 (2016).
- [6] Wypych G, “Handbook of Material Weathering” Toronto- New York: ChemTec Publishing, 2003, pp. 61–63.

MODELLING

Gradient Material Model in Analysis of Mechanical Joints

The constant attempt to obtain as low aircraft mass as possible is the reason for using materials of high specific strength and stiffness in the aerospace industry. High strength steels, titanium or aluminum alloys (e.g. 2024-T3) and composite laminates (e.g. CFRP or FML) are the examples of such materials.

Mechanical joints used for decades are proved to be reliable. They can be assembled and applied in very rough conditions since they are less sensitive to environmental effects. Therefore, they are still employed in aircraft design. Hole drilling is a (necessary) stage in manufacturing of a mechanical joint. Laminates are notch sensitive materials. Hole vicinities are the areas of high stress concentrations so they determine load capability of the whole structure. Therefore, mechanical joints of composite parts require a special attention to be focused during both the designing and manufacturing process.

The analysis is performed on the specimen in the form of a double-shear bolted joint with four steel fasteners. The outer elements are made of 2024-T3 aluminum alloy sheet and the inner element is made of quasi-isotropic CFRP laminate consisting of UD laminate layers (HTA/913) and external fabric layers (TR30S twill woven) with [(0)/0/45/90/45/0/45/90/45/0/90]S stacking sequence.

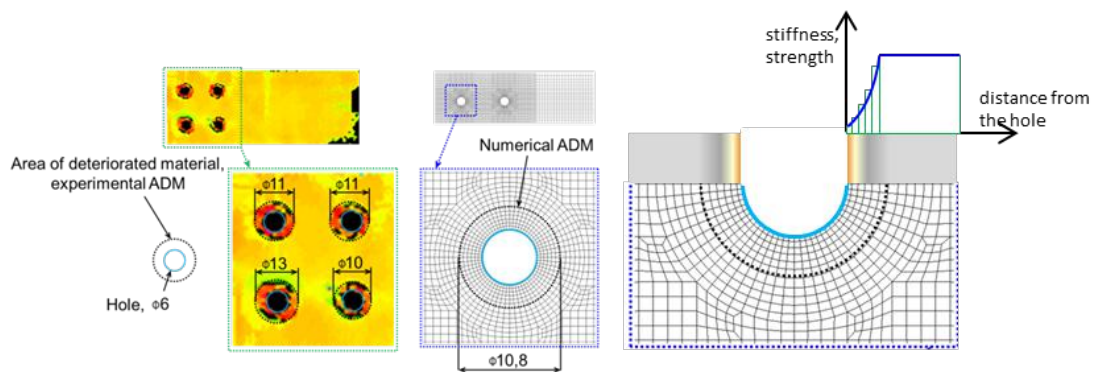


Figure 7. Results of NDT analysis and idea of gradient material model

Defects of the laminate coupon around the hole, caused by drilling process, constitute an area of weakened/deteriorated material (ADM). It was identified using NDT method. The average diameter of those areas in analyzed laminate coupon equals about 11 mm. The exemplary results of the NDT tests and corresponding ADM in finite element model are presented in Figure 7.

Consideration of initial delamination only between prepreg layers (without any changes of prepreg/lamina properties) does not sufficiently affect the results. This leads to the conclusion that the drilling process has caused a significant deterioration of prepreg/lamina properties around the hole. Lamina properties are thought to be changing gradually in this area, therefore, simple gradient material model was applied to describe this phenomenon. ADM was divided into zones having different values of material properties (stiffness and strength components). Several cases of decomposition of ADM (in the hole vicinity) were analyzed. The function of gradient material is unknown and cannot be determined experimentally, therefore a series of numerical models was analyzed to estimate it.